Immunization with mannosylated nanovaccines and inhibition of the immune-suppressing microenvironment sensitizes melanoma to immune checkpoint modulators

This is the author copy of the original published in *Nat. Nanotechnol.* **14,** 891–901 (2019)
(https://doi.org/10.1038/s41565-019-0512-0 https://www.nature.com/articles/s41565-019-0512-0

Ibrutinib sensitizes melanoma to immune checkpoint modulators following immunization with nano-vaccines by relieving immune-suppressing microenvironment

One Sentence Summary:

Combination of dendritic cell-targeted nano-vaccines with a myeloid-derived suppressor cell inhibitor and immune checkpoint modulators expands the host antitumor immune cells, restricts tumour growth and prolongs survival in an orthotopic melanoma model.

João Conniot,[1,2¥] Anna Scomparin,[1,3¥] Carina Peres,[2] Eilam Yeini,[1] Sabina Pozzi,[1] Ana I Matos,[2] Ron Kleiner,[1] Liane IF Moura,[2] Eva Zupančič,[2,4] Ana S Viana,[5] Hila Doron,[6] Pedro MP Gois,[2] Neta Erez,[6] Steffen Jung,[4] Ronit Satchi-Fainaro,[1*] Helena F Florindo[2*]

[1]Department of Physiology and Pharmacology, Sackler Faculty of Medicine, Tel Aviv University, Tel Aviv, Israel

[2] Research Institute for Medicines (iMed.ULisboa), Faculty of Pharmacy, Universidade de Lisboa, Lisbon, Portugal

[3] Department of Drug Science and Technology, University of Turin, Turin, Italy

[4] Department of Immunology, Weizmann Institute of Science, Rehovot, Israel

[5] Center of Chemistry and Biochemistry, Faculty of Sciences, Universidade de Lisboa, Lisbon, Portugal

[6] Department of Pathology, Sackler Faculty of Medicine, Tel Aviv University, Tel Aviv 69978, Israel

[¥]These authors equally contributed to this work
*Corresponding authors:

Helena F Florindo, hflorindo@ff.ulisboa.pt
Ronit Satchi-Fainaro, ronitsf@tauex.tau.ac.il

Keywords: vaccine, melanoma, ibrutinib, MDSC inhibitor, PD-1, OX40, nanomedicines.

ABSTRACT

Low response rate, acquired resistance, and severe side effects have limited the clinical outcomes of immune checkpoint therapy. Here we show that combining cancer nano-vaccines with anti-PD-1 for immunosuppression blockade, and anti-OX40 for effector T cell stimulation, expansion, and survival, can potentiate the efficacy of melanoma therapy. Prophylactic and therapeutic combination regimens of dendritic cell-targeted mannosylated nano-vaccines with anti-PD-1/anti-OX40 (αPD-1/αOX40) demonstrate synergism, stimulating T cell infiltration into tumours at early treatment stages. However, treatment at the therapeutic regimen does not result in enhanced inhibition of tumor growth compared to αPD-1/αOX40 alone and is accompanied by increased infiltration of myeloid-derived suppressor cells (MDSC) in tumours. Combining the double therapy with ibrutinib, an MDSC-inhibitor, leads to remarkable tumour remission and prolonged survival in treated melanoma-bearing mice. The synergy between the mannosylated nano-vaccines, ibrutinib and αPD-1/αOX40 provides essential insights to devise alternative regimens to improve the efficacy of immune checkpoint modulators in solid tumours by regulating the endogenous immune response.

INTRODUCTION

Advances in immunotherapy have improved the treatment outcomes of melanoma, based on antitumor immune responses elicited by the patient's own immune system. Cytotoxic T lymphocyte-associated protein-4 (CTLA-4) and programmed cell death protein 1 (PD-1) blockade have enhanced specific T cell-mediated antitumor immunity in clinical practice [1,2]. Since these findings, efforts are being made not only to inhibit negative immune checkpoints but also to stimulate activation signalling pathways of the immune system. For example, OX40 (CD134 or TNFSFR4) is a co-stimulatory receptor member of the tumour necrosis factor (TNF) family that is transiently expressed on activated T cells. Once activated, OX40 induces expansion, trafficking, and survival of effector T cells, and increases pro-inflammatory cytokine secretion [3,4]. OX40-signaling can also block the inhibitory activity of tumour-infiltrating regulatory $CD4^+$ T cells, by hindering Foxp3, TGF-β, and IL-10 signalling, known to suppress vaccine-induced immune responses [5-7].

Despite the promising clinical results, immune checkpoint therapy has been associated with low percentages of effective and durable responses to single agent therapies, due to resistance or relapse [8-10]. The presence of tumour infiltrating lymphocytes (TIL) has been correlated with favourable outcomes of immune checkpoint modulation therapies [11]. Based on these observations, and in an effort to integrate a novel therapeutic approach, we hypothesized that cancer vaccines delivering tumour-associated antigens to dendritic cells (DC) and consequent T-cell priming and activation, could potentiate the antitumor responses and survival outcomes of the combination of PD-1 blockade and OX40 co-stimulation. Therefore, we set to test this hypothesis in two murine models of melanoma.

In order to modulate the generation and function of myeloid-derived suppressor cells (MDSC), we further administered ibrutinib, an irreversible inhibitor of Bruton's tyrosine kinase (BTK). Under cancer-associated inflammation, an aberrant myelopoiesis leads to the accumulation of MDSC, compromising the efficient maturation of DC, affecting the antigen presentation process and driving T cell transcriptional programs towards T cell anergy and exhaustion. The presence of MDSC has been also correlated to decreased efficacy of anti-CTLA-4, constituting an important target for enhancing the efficacy of immune checkpoint inhibitors [12,13].

Here, we report the design, synthesis and characterization of biodegradable polymeric nano-sized particles made of mannose-grafted polylactic-co-glycolic acid/polylactic acid (PLGA/PLA) (man-NP) (**Fig. 1A**). Man-NP were designed to improve the nanoparticle interactions with DC by targeting the mannose receptor (MR/CD206) [14]. The mannosylated nano-vaccines contained the Toll-like receptor (TLR) ligands CpG and monophosphoryl Lipid A (MPLA), as immune potentiators, and the melanoma-associated melan-A/MART-1 peptides as antigens. The mannosylated nano-vaccines carried short (10 amino acids) and long (20 amino acids) melan-A/MART-1 peptides, aiming for the major histocompatibility complex (MHC) class I and class II antigen presentation pathways, respectively. Melan-A/MART-1 (26-35(A27L)) MHCI-restricted peptide (MHCI-ag) and melan-A/MART-1 (51-73) MHCII-restricted peptide (MHCII-ag) were used. Activation of MHC class I and MHC class II potentiated these active vaccination strategies, by engagement of both $CD4^+$ and $CD8^+$ T cells [15].

Our results demonstrate amplified antitumor immune response mediated by (i) targeting DC through vaccination as an active immunotherapy, (ii) inhibiting MDSC, and (iii) modulating OX40 and PD-1 on T cells. Here we show that this strategy led to

DC recruitment and differentiation to re-shape the tumour microenvironment (TME) cellular plasticity and induced a remarkable melanoma growth inhibition.

RESULTS

Polymeric nanoparticles as antitumor nano-vaccines

To deliver tumour-associated antigens to DC, we developed two different types of biodegradable nanoparticles: PLGA/PLA NP (NP) and mannose-PLGA/PLA NP (man-NP) (**Fig. 1A**). To prepare man-NP, mannose-grafted PLGA polymer was synthesized by amidation of the terminal carboxylic acid groups of PLGA with mannosamine [16]. The reaction was confirmed by ^{1}H NMR of mannose-PLGA (**Supplementary Fig. 1**) compared with the individual ^{1}H NMR spectra of mannosamine and PLGA. The multiplet signal between 3.2 and 3.8 ppm indicates the presence of mannose in the mannose-PLGA polymer, as previously reported [17]. NP and man-NP were prepared by the double emulsion solvent evaporation method [18]. The average hydrodynamic diameters of NP and man-NP were similar and ranged between 166 ± 5 nm and 181 ± 8 nm, depending on the entrapped molecules (**Table 1**), with a low polydispersity index (0.13 ± 0.04 to 0.18 ± 0.04). Electron microscopy and atomic force microscopy showed homogenous spherical particles, with slight roughness on the surface (**Fig. 1B, C, D**) and near-neutral surface charge (**Table 1**). Mannose residues on the surface of man-NP were detected by the Lectin Recognition Assay, using Concanavalin A (Conc A) (**Supplementary Fig. 2A**). Conc A binds to exposed mannose residues, forming aggregates [15,19]. After incubation of man-NP, Conc A induced particle aggregation, revealed by a 5-fold increase in average size (**Supplementary Fig. 2B**). Particle aggregation (in green) was also confirmed by fluorescence microscopy following incubation of fluorescein isothiocyanate (FITC)-

labelled Conc A with man-NP (**Supplementary Fig. 2C**). Non-mannosylated NP were the negative control.

NP and man-NP showed high levels of entrapment efficiency (EE) and loading capacity (LC) (**Table 2**). For the MHCI-ag, EE >97.5 ± 0.2% and LC >48.8 ± 0.1 µg/mg, while for the MHCII-ag EE >74.6 ± 3.5% and LC >37.3 ± 1.7 µg/mg. The EE of CpG was above 80.8 ± 2.5%, which corresponds to LC of 8.1 ± 0.3 µg/mg.

NP and man-NP did not affect DC viability (>90%) in the concentration range tested (**Supplementary Fig. 3A**), supporting their physiological biocompatibility. This was also assessed *ex vivo* by red blood cell (RBC) lysis determination. NP and man-NP did not disrupt RBC membranes at concentrations up to 20 mg/ml (**Supplementary Fig. 3B**).

Mannosylated nano-vaccines are highly internalized by dendritic cells

To determine internalization, Cy5.5-labeled NP and man-NP were incubated with murine immature dendritic cells (JAW SII). FACS measurements showed higher uptake with increasing time of contact. Man-NP exhibited much higher internalization levels (P = 0.001) than non-mannosylated NP (**Fig. 1E**). Particle internalization was also confirmed by confocal microscopy, corroborating the FACS results (**Fig. 1F).** Cy5.5-labeled NP and man-NP prepared with PVA instead of TPGS were used as control. We observed a dramatic increase in NP uptake while using TPGS compared with PVA, including those NP functionalized with mannose (**Supplementary Fig. 4**). The higher uptake obtained for mannosylated NP (TPGS) was reduced in the presence of soluble mannose, which confirms that the higher internalization obtained for mannose-decorated NP was mediated by the interaction of this targeting moiety with CD206 receptor at the DC surface.

We show that our man-NP (TPGS) was preferentially taken-up *in vivo* by circulating DC (gated as $CD11b^{+}CD11c^{+}$), compared to macrophages ($CD11b^{+}CD11c^{-}$) and resident DC ($CD11b^{-}CD11c^{+}$) (**Fig. 1G, Supplementary Fig. 5**). In addition, our nano-vaccine was able to significantly increase the expression of activation/maturation markers at the surface of these APC (**Fig. 1H**).

Mannosylated nano-vaccines induce splenocyte activation and cytotoxicity against melanoma cells

After subcutaneous (s.c.) injection of Cy5.5-labeled NP or man-NP (20 mg/ml), 50 μl in the right hind and 50 μl in the left hind, particles remained at the site of immunization 48 hours following injection ($N = 4$). Fluorescence signal measurements revealed the preferential accumulation of particles in the lymph nodes (LN). Residual accumulation was detected in the liver and the kidney, due to the excretion of metabolic particle derivatives (**Fig. 2A-B**).

To determine the ability of NP and man-NP to induce specific immune responses, we performed a 3-time immunization, seven days apart, to C57BL/6J mice. Ten days after the last immunization, splenocytes were harvested and re-activated in cell culture for 6 days with anti-CD28 and MHCI-ag alone, or in combination with MHCII-ag (**Fig. 2C**). The groups treated with NP and man-NP showed an increased secretion of inflammatory cytokines, such as IFN-γ, a Th1 cytokine, and GM-CSF. The highest levels of IFN-γ and GM-CSF were induced by man-NP. Elevated levels of CCL1/TCA-3 and TARC/CCL17 also suggested that our particles played a major role in priming antigen-specific T cells (**Fig. 2D**). There was no evidence of body weight change in all groups, attesting to vaccine tolerability and safety (**Supplementary Fig. 6**).

Analysis of Th2 cytokines revealed that the administration of NP MHCI-ag/NP MHCII-ag and man-NP MHCI-ag/man-NP MHCII-ag decreased MIP-1β/CCL4 secretion, whereas both man-NP MHCI-ag and the combination man-NP MHCI-ag/man-NP MHCII-ag equally reduced the MCP-5/CCL12 levels. These results indicate the role of nanoparticulate vaccines in the modulation of Th2 chemokine secretion profile.

The major goal of a successful antitumor immunotherapy is to trigger antigen-specific cytotoxic $CD8^+$ T cells (CTL) to recognize and destroy target cells. Splenocytes collected from mice immunized with man-NP MHCI-ag/man-NP MHCII-ag exhibited the highest *ex vivo* cytotoxicity when co-cultured with mCherry-labelled murine Ret melanoma cells (RMS) (**Fig. 2E**). These data suggest that the immunization with man-NP MHCI-ag or man-NP MHCI-ag/man-NP MHCII-ag efficiently triggered CTL responses. Man-NP MHCI-ag/man-NP MHCII-ag elicited the highest CTL activity. These were superior to man-NP MHCI-ag (P = 0.014), to non-mannosylated NP co-entrapping both antigens (P = 0.02), and dramatically stronger than NP MHCI-ag/MHCII-ag (P = $9.6x10^{-6}$). MHCI-ag/MHCII-ag/CpG/MPLA (free antigen/immune potentiators) or empty particles induced a CTL activity similar to PBS (**Fig. 2E**).

The CTL activity induced by man-NP MHCI-ag/man-NP MHCII-ag is clearly shown by the increased fluorescent staining related to caspase 3/7 activation (in green), a marker of apoptosis (**Fig. 2F**).

Prophylactic mannosylated nano-vaccines synergize with anti-PD-1/anti-OX40 (αPD-1/αOX40) treatment, restricting melanoma growth and prolonging survival

Given the *in vitro* and *ex vivo* findings, we next asked whether the immune response elicited by the mannosylated nano-vaccines would synergize with the PD-1 blockade and OX40 activation for melanoma therapy. To test this hypothesis, mice were treated according to the schedule in **Fig. 3A**. When man-NP MHCI-ag/man-NP MHCII-ag was combined with αPD-1/αOX40, a remarkable tumor growth inhibition was obtained (**Fig. 3B-E, Supplementary Fig. 8**), with minimal systemic toxicity (**Supplementary Fig. 7**).

At day 17 after tumour cell inoculation, the tumour volume in animals treated with αPD-1/αOX40, or with the combination of non-mannosylated (NP MHCI-ag/NP MHCII-ag) or mannosylated nano-vaccines (man-NP MHCI-ag/man-NP MHCII-ag) with αPD-1/αOX40 was much lower compared to animals treated with PBS ($P < 0.0016$) (**Fig. 3D**). At day 27, the tumour volume intra-group variability increased for all the groups, except for the one treated with the combination of man-NP MHCI-ag/man-NP MHCII-ag + αPD-1/αOX40, in which the tumours remained small (**Fig. 3E, Supplementary Fig. 8**). Empty NP, with and without mannose were used as controls. Tumour volumes of animals vaccinated with empty NP or empty man-NP were similar to those treated with PBS (**Supplementary Fig. 8**).

Of note, the combination of mannosylated nano-vaccines with αPD-1/αOX40 induced a prolonged overall survival. The combination man-NP MHCI-ag/man-NP MHCII-ag + αPD-1/αOX40 resulted in 100% survival 42 days following tumour inoculation, with a survival rate of 50% two months following tumour inoculation. On

the other hand, treatment with αPD-1/αOX40 resulted in only 20% of survival (**Fig. 3C**).

Immunohistochemistry staining revealed high levels of caspase-3 and tumour-infiltrating $CD4^+$ and $CD8^+$ T cells in all groups immunized with nano-vaccines (**Supplementary Fig. 9**). The highest level of $CD8^+$ T cell infiltration was observed in groups treated with mannosylated nano-vaccines, alone or in combination with αPD-1/αOX40, and non-mannosylated nano-vaccines alone, suggesting that indeed the nano-vaccines are capable of reactivating cell-mediated cytotoxicity in the TME (**Supplementary Fig. 9**).

Combination of therapeutic nano-vaccines with αPD-1/αOX40 immune checkpoint therapy at an intervention dosing schedule

Motivated by the synergism observed with the combination of prophylactic nano-vaccines with αPD-1/αOX40, we hypothesized that the same antitumor immune-mediated effect could be achieved by treating melanoma-bearing mice at a therapeutic regimen. Therefore, man-NP MHCI-ag/man-NP MHCII-ag were combined with αPD-1/αOX40 according to the dosing schedule described in **Fig. 4A** and tested in Ret melanoma cells and mCherry-labelled Ret melanoma (RMS) cells. mCherry-labelling of Ret cells did not alter tumour cell proliferation, neither *in vitro* (data not shown) nor *in vivo*. Ret cells and RMS induced similar tumour growth profiles in C57BL/6J mice, and the response to our triple combination therapies, man-NP MHCI-ag/man-NP MHCII-ag + αPD-1/αOX-40 + ibrutinib, was also similar (**Supplementary Fig. 10**).

The groups αPD-1/αOX40 and man-NP MHCI-ag/man-NP MHCII-ag + αPD-1/αOX40 showed similar average tumour volume at day 18, which was 6-fold

significantly smaller compared to the PBS-treated ($P < 0.0012$) (**Fig. 4B**), with negligible systemic toxicity observed (**Supplementary Fig. 11**).

On day 18 after tumour inoculation, the combination of mannosylated nano-vaccines with αPD-1/αOX40 did not result in further tumour growth restriction compared to αPD-1/αOX40 alone; however, the animals treated with the combination had the highest levels of $CD8^+$ T cells in tumour infiltrates ($P < 0.001$) (**Fig. 4D, Supplementary Fig. 12**). These data support the synergism we previously observed in the prophylactic regimen.

The treatment with αPD-1/αOX40 induced the lowest levels of $CD4^+$ T-cell infiltrates (**Fig. 4E, Supplementary Fig. 12**) displaying reduced infiltration of regulatory T (Treg) cells (**Fig. 4F, Supplementary Fig. 13**). Animals treated with the mannosylated nano-vaccines, alone or in combination, had higher levels of Treg cells compared to αPD-1/αOX40-treated group. Therefore, the highest CD8:Treg ratio was observed for αPD-1/αOX40 treatment, followed by the combination of mannosylated nano-vaccines with αPD-1/αOX40 immune checkpoint therapy (**Fig. 4G**).

At the final endpoint, the animals treated with αPD-1/αOX40 remained with the highest CD8:Treg ratio. This was 7-fold higher compared to the groups treated with mannosylated nano-vaccines, alone or in combination with αPD-1/αOX40 ($P < 0.01$).

Interestingly, from day 18 to the final endpoint, the infiltration of $CD11b^+Gr\text{-}1^+$ MDSC increased significantly in the two groups treated with mannosylated nano-vaccines, alone or in combination (**Fig. 4H, Supplementary Fig. 14**). At the final endpoint, the levels of MDSC in those groups were approximately 4-fold higher than those obtained for the αPD-1/αOX40-treated group. These extremely elevated levels of MDSC seem to correlate with the marked decrease of $CD8^+$ T cell infiltration (**Fig. 4D, Supplementary Fig. 12**) and with the high percentage of Treg cells (**Fig. 4F,**

Supplementary Fig. 13) at the final endpoint in the two groups treated with the mannosylated nano-vaccine. This contributes to lower CD8:Treg ratios at the final

Trivalent combination of mannosylated nano-vaccines with ibrutinib and αPD-1/αOX40 strongly restricts melanoma growth and prolongs overall survival

Considering the high levels of MSDC observed in the tumour infiltrates, we hypothesized that combined targeted inhibition of these cells with our mannosylated nano-vaccines and immune checkpoint modulators would lead to enhanced therapeutic efficacy. To inhibit MDSC, we selected ibrutinib, an irreversible inhibitor of the Bruton's tyrosine kinase (BTK) and interleukin-2-inducible T-cell kinase (ITK), which can modulate the generation and function of MDSC [20,21].

Melanoma-bearing mice were treated according to the schedule in **Fig. 5A**. On day 20 after tumour inoculation, we observed that the average tumour volume of groups treated with ibrutinib or with mannosylated nano-vaccines + ibrutinib were identical to the PBS-treated group. In the groups treated with mannosylated nano-vaccines + αPD-1/αOX40 or αPD-1/αOX40 + ibrutinib, however, the tumour volume was significantly reduced by more than 5-folds (P = 0.038 and P = 0.0060, respectively) (**Fig. 5B)**. In addition, the mannosylated nano-vaccines (man-NP) were significantly superior to the non-mannosylated nano-vaccines (NP) from day 19 onwards (P = 0.005), demonstrating the crucial role of the mannose targeting moieties for achieving an effective immune-mediated control of tumour growth (**Supplementary Fig. 15A-B**). In fact, on day 23, the man-NP-treated group had an average tumour volume of 54 mm^3, in contrast to the NP-treated group, which had an average tumour volume of 638 mm^3.

The trivalent therapy, comprising of the combination of mannosylated nano-

vaccines induced the most potent specific anti-tumour immune response (P = 0.001) (**Fig. 5C-D, Supplementary Fig. 15C-D**). The superior antigen-dependent immune response was irrespective of the antigen used (gp100 or melan-A/MART-1) as shown by a tetramer staining assay (**Fig. 5C**, **Supplementary Fig. 15C-D**). Melan-A/MART-1 specificity was further confirmed by the IFN-γ ELISpot assay **(Supplementary Fig. 15E).** The highest levels of antigen-specific intracellular IFN-γ$^+$ stained in tumour-infiltrating cytotoxic CD8$^+$ T lymphocytes of RMS-bearing mice measured by FACS, at the 1st endpoint, were obtained for animals treated with the mannosylated nano-vaccines (**Supplementary Fig. 15F**).

On day 33, animals treated with the man-NP MHCI-ag/man-NP MHCII-ag + αPD-1/αOX40 + ibrutinib presented a 3-fold higher survival percentage (P = 0.0049) compared to animals treated with NP MHCI-ag/NP MHCII-ag + αPD-1/αOX40 + ibrutinib, among which 8 out of 13 already reached a tumour volume of at least 1000 mm^3 (**Supplementary Fig. 15G**).

Fourteen out of 15 animals of the group mannosylated nano-vaccine + αPD-1/αOX-40 + ibrutinib remained alive at day 40, in comparison to 7 out of 15 animals of the group αPD-1/αOX-40 + ibrutinib (**Fig. 5E**). These animals treated with αPD-1/αOX-40 + ibrutinib presented higher variability in terms of tumour size (**Fig. 5F**). Moreover, 7% of the animals treated with mannosylated nano-vaccine + αPD-1/αOX-40 and 23% of the animals treated with αPD-1/αOX-40 + ibrutinib remained alive after 65 days, while 67% of animals treated with the trivalent combination mannosylated nano-vaccine + αPD-1/αOX-40 + ibrutinib survived during that period. The survival curves of the triple regimen are statistically different from those obtained for PBS (P = 0.0001), man-NP + αPD-1/αOX-40 (P = 0.0001) and αPD-1/αOX-40 + ibrutinib (P

= 0.0256) treatments. Furthermore, we detected only slight body weight changes relative to the initial body weight, throughout the study, reflecting negligible systemic toxicity (**Supplementary Fig. 11**).

We determined two endpoints to analyse immune cell infiltrates within the TME. The first endpoint, day 20 after tumour inoculation, corresponds to the day of the first death in the PBS-treated group, whereas the second endpoint was tumour size-matched, occurring on day 27 for PBS, ibrutinib only and mannosylated nano-vaccines + ibrutinib, and on day 35 for αPD-1/αOX40 + ibrutinib and mannosylated nano-vaccines + αPD-1/αOX40. During this period, the tumours of animals treated with mannosylated nano-vaccines + αPD-1/αOX40 + ibrutinib were very small and therefore, those were kept for the immunohistochemistry (IHC) analysis.

Higher infiltration of T lymphocytes, as expected, was associated with stronger tumour growth inhibition (**Fig. 6A, Supplementary Fig. 12**). The number of $CD8^+$ T lymphocytes was more than 20-fold higher for mice treated with αPD-1/αOX40 + ibrutinib or with mannosylated nano-vaccines + αPD-1/αOX40, compared to the PBS-treated group (**Fig. 6B, Supplementary Fig. 12).**

The highest level of $CD8^+$ TIL, at the second endpoint, was induced by αPD-1/αOX40 + ibrutinib. At this time point, low levels of Treg cells were observed within the tumours of animals treated with αPD-1/αOX40 + ibrutinib or mannosylated nano-vaccines + αPD-1/αOX40 (**Fig. 6D, Supplementary Fig. 13**). Both treatments also resulted in high CD8/Treg ratios, which correlated with the enhanced therapeutic efficacy (**Fig. 6E**).

IHC staining of RMS tumour sections for CD4 and CD8 confirmed the flow cytometry results, showing a prominent infiltration of $CD8^+$ T cells at day 20 after tumour inoculation, in groups that received the mannosylated nano-vaccines with

αPD-1/αOX40. The mannosylated nano-vaccines also induced higher expression of the OX40 receptor as shown in the groups treated with man-NP MHCI-ag/man-NP MHCII-ag + ibrutinib and man-NP MHCI-ag/man-NP MHCII-ag + αPD-1/αOX40 (**Supplementary Fig. 16**). It should be noted that the expression of PD-1/PD-L1 was the lowest for the tumours of animals treated with man-NP MHCI-ag/man-NP MHCII-ag + αPD-1/αOX40 + ibrutinib, even compared to those immunized with the non-mannosylated NP (**Supplementary Fig. 17**).

High levels of caspase-3 were observed in the tumours of the groups that received man-NP MHCI-ag/man-NP MHCII-ag + ibrutinib, man-NP MHCI-ag/man-NP MHCII-ag + αPD-1/αOX40 and αPD-1/αOX40 + ibrutinib, although only man-NP MHCI-ag/man-NP MHCII-ag + αPD-1/αOX40 and αPD-1/αOX40 + ibrutinib strongly inhibited tumour growth and significantly prolonged survival of the mice (**Fig. 5B, Fig. 5E, Supplementary Fig. 16**).

In groups treated with αPD-1/αOX40 + ibrutinib, and mannosylated nano-vaccines + ibrutinib, we observed a decrease in MDSC infiltrates from the first to the second endpoint. This suggests that ibrutinib was restricting the migration of MDSC into the TME (**Fig. 6G, Supplementary Fig. 14, Supplementary Fig. 17**).

The trivalent combination showed superior antitumor efficacy also in two independent studies (*N* = 6-9/group in each experiment) using a second mouse model bearing orthotopic s.c. B16-F10 melanoma (**Supplementary Fig. 18**). In this case, the dosing regimen led to 79% (first study **Supplementary Fig. 18A**) and 81% (second study **Supplementary Fig. 18B**) tumour growth inhibition at day 19 for the combination of mannosylated nano-vaccines with ibrutinib and αPD-1/αOX40, *versus* 67% (**Supplementary Fig. 18A**) and 68% (**Supplementary Fig. 18B**) for the nano-

vaccines + αPD-1/αOX40 combination *versus* 70% (**Supplementary Fig. 18A**) and 57% (**Supplementary Fig. 18B**) for the αPD-1/αOX-40 + ibrutinib combination. The proposed mechanism was confirmed in this second melanoma model by the reduction of infiltrating MDSC and the increase of infiltrating T cells in the TME (**Supplementary Fig. 19**). We selected Day 19 for comparison as this is the last day of the studies at which all the animals in all the groups were still present.

DISCUSSION

The recent clinical validation of different immune checkpoint modulators has revolutionized cancer therapy. However, low response rate, adverse effects and resistance led to the clinical need for alternative combination strategies to overcome these limitations [22].

Our results report the synergism of mannosylated antitumor nano-vaccines with ibrutinib and PD-1 blockade/OX40. Our trivalent treatment strategy re-established the dynamic equilibrium between the host effector antitumor immunity and the tumour-mediated evasion mechanisms, based on the modulation of immune cell activity within the TME, rather than the direct effect on tumour cells. This resulted in a remarkable restriction of melanoma growth and long-term survival (**Fig. 7**).

These nano-vaccines, as an active immunotherapeutic strategy, have the unique ability to expand host antitumor specific T effector phenotype, improving sensitivity and long-term tumour recognition. The synergistic effect between αPD-1/αOX40, already reported in an ovarian cancer model [23], could be relevant for melanoma [24] and be potentiated by cancer vaccines delivering tumour-associated antigens to DC.

We designed and synthesized non-mannosylated (NP) and mannosylated nano-vaccines (man-NP) for the *in vivo* co-delivery of melanoma-associated antigens (MAA) and TLR agonists to DC, via phagocytosis-dependent ("passive") and ligand-mediated ("active" through the mannose receptor (MR/CD206)) targeting, respectively. The two different particles were biocompatible and had similar morphology and physico-chemical characteristics in terms of size, PdI, surface charge, EE, and LC. Intravital imaging revealed that NP and man-NP remained near the site of injection, after s.c. hock immunization, promoting contact with DC at the periphery (inguinal lymph node), as well as proximity to the popliteal and axillary lymph nodes. These data explain the preferential accumulation of the nano-vaccines in these tissues, which is extremely important for the induction of antigen-specific adaptive immune responses and vaccine efficacy [25]. The mean average diameter of these nano-vaccines, below 200 nm, may also be suitable for their trafficking through the lymphatic drainage directly to the lymphoid organs [26]. Despite the similar biodistribution profiles, mannosylated man-NP were much more efficiently internalized by DC compared to non-mannosylated NP (P = 0.00067). The mannose residues on the surface of man-NP, demonstrated by particle aggregation induced by Conc A, increased particle affinity to MR/CD206 of DC, improving particle internalization [14]. The added value of mannose grafted onto the surface of our nano-vaccine was further confirmed *in vitro*, as the soluble mannose in the medium significantly reduced the mannose-mediated NP internalization by DC.

The most important goal of antitumor vaccination is the induction of cytotoxic activity against tumour cells. The presence of mannose on the surface and the particulate nature of our nano-vaccines carrying MAA and TLR agonists, played a pivotal role in this process, by activating splenocytes in healthy animals. While the

same MAA and TLR agonists, administered freely, only induced a negligible immune response. The co-delivery of tumour-associated antigens and TLR ligands by the same nanoparticulate carrier enhances antigen internalization, processing, and subsequent presentation. This is a key step to overcome host tolerance to tumour cells by improving effective T cell priming and lymphocyte expansion [15].

Recently, the TLR synergy has been reported [27] showing that their activation on DC is crucial to induce tumour-specific T cell responses [28]. The role of TLR4 agonists (MPLA) on Treg cells is underexplored, but it was shown to be essential for the immune-mediated destruction of cancer cells [29]. CpG, a TLR9-agonist, on the other hand, was shown to suppress the activation of those Treg cells, increase $CD4^+$ T cell survival, and promote the infiltration of $CD8^+$ T cells into the tumour [30]. Our nanoparticles allowed the multi-targeting TLR co-stimulatory effect, by entrapping both CpG and MPLA within the same polymeric matrix, in contrast to their free administration. The co-delivery of these TLR agonists to a single DC potentiates the efficient maturation of these cells towards balanced Th1- and Th2-type immune responses, which are crucial to control homeostasis within the tumour site [31,32]. It was previously reported that the intra-tumour administration of CpG, in combination with αOX40, induced a superior antitumor effect in melanoma compared to each of these agonists alone [33]. Our nano-platforms constitute an alternative for the targeted delivery of CpG oligonucleotide, as the *ex vivo* and *in vivo* studies presented here support the successful protection of CpG, once entrapped within our nano-vaccines polymeric matrix.

Mannosylated and non-mannosylated nano-vaccines triggered the secretion of pro-inflammatory cytokine profiles. We observed a significant increase in the secretion of IFN-γ and GM-CSF, after re-stimulating the splenocytes collected from

mice treated with nano-vaccines. IFN-γ and GM-CSF are associated with enhanced antigen priming and subsequent presentation by antigen-presenting cells (APC) [34,35], as well as cytotoxic T cell activity. IFN-γ is extensively produced by $CD8^+$ T cells and it is a predictor of antigen-specific cytotoxic T cell-mediated responses [36]. The increased activation of $CD8^+$ T cells in mice treated with nano-vaccines is also supported by the increased secretion of CCL1/TCA-3 and TARC/CCL17, which are chemokines associated with activated T cells [37,38].

An inclusive assessment of the triad, IFN-γ, IL-2 and TNF-α, predicted an improved CTL activity for man-NP MHCI-ag/man-NP MHCII-ag. We also observed that our nano-vaccines increased the secretion of IL-6, which is involved in the recruitment and differentiation of T lymphocytes, as well as in the suppression of Treg cells [39,40]. The suppression of these cells is important for eliciting CTL cell activity triggered by our nano-vaccines. Furthermore, the decreased secretion of MIP-1β/CCL4 and CCL12, as detected in the splenocytes from animals treated with our nano-vaccines, has also been associated with the inhibition of Treg cells, reduction of tumour angiogenesis and enhanced antitumor efficacy [41,42].

The pro-inflammatory cytokine secretion profile induced by our nano-vaccines clearly correlated with increased *ex vivo* CTL activity. Man-NP carrying MHCI-ag and MHCII-ag induced the most robust CTL activity against murine RMS cells *ex vivo*. The benefit of MHC class II peptides in cancer vaccination, however, is still unclear. In clinical trials, it has been associated with poor prognosis, due to increased activity of $CD4^+CD25^+$ Treg cells or apoptosis of activated $CD8^+$ T cells [43,44]. Our results, on the contrary, support that the engagement of synergistic MHCI and MHCII responses can lead to stronger $CD8^+$ cytotoxic T cell responses [45]. Man-NP with MHCI-ag and MHCII-ag not only induced the strongest *ex vivo* CTL activity, but also slightly

enhanced antitumor immunity *in vivo*, when compared to treatment with man-NP carrying only MHCI-ag.

Our prophylactic nano-vaccines alone, as expected, induced a modest tumour growth inhibition *in vivo*. This is in agreement with the poor to moderate efficacy reported for cancer vaccines, due to tumour aggressiveness and the immunosuppressive TME [46]. The combination of prophylactic man-NP MHCI-ag/man-NP MHCII-ag with αPD-1/αOX40, however, highlights the synergistic antitumor effect of these complementary approaches. This combination resulted in the most potent antitumor response, leading to a survival of 50% of the mice for more than 2 months following tumour inoculation. We observed only minimal and yet reversible systemic toxicity, reflected by slight body weight change relative to the initial body weight.

The use of MHCI-ag and MHCII-ag peptides was essential for the induction of a robust antitumor response. The nano-platform was also crucial, as the free administration of the same MAA induced much lower efficacy. The combination of MHCI-ag/MHCII-ag (free) + αPD-1/αOX40 induced 20% survival, similar to αPD-1/αOX40 alone. This survival rate is 30% lower compared to the combination of mannosylated nano-vaccines (man-NP MHCI-ag/man-NP MHCII-ag) + αPD-1/αOX40.

Antitumor activity was achieved solely in those groups that were treated with antigen-loaded NP, as opposed to those treated with empty NP. This is an indication that the immune-mediated effect obtained with NP entrapping antigens resulted from the increased immunogenicity of those epitopes conferred by the adjuvant effect of our nano-vaccine.

The tumours collected from mice treated with the combination prophylactic man-NP MHCI-ag/man-NP MHCII-ag + αPD-1/αOX40 had extensive infiltration of

$CD8^+$ T cells, a good prognosis marker for immunotherapy. We also observed increased caspase-3 levels in these tumours, correlating with the superior CTL activity observed *ex vivo*.

The remarkable results achieved with the combination of prophylactic mannosyated nano-vaccines (man-NP MHCI-ag/man-NP MHCII-ag) + αPD-1/αOX40 prompted the design of a therapeutic intervention strategy. Therapeutic mannosylated nano-vaccines (man-NP MHCI-ag/man-NP MHCII-ag), rather than prophylactic, increase the applicability of the strategy and the chances for translation to the clinic. Clinical studies combining antitumor cellular vaccines with immune checkpoint therapy have had promising outcomes in pancreatic cancer [47], colorectal cancer [48], prostate cancer [49] and melanoma [50]. Our therapeutic strategy could offer a clinical alternative to those therapies with autologous DC, which are associated with complex, long and expensive procedures [51].

In the beginning of the treatment, the combination of mannosylated nano-vaccines + αPD-1/αOX40 clearly increased the tumour infiltration of $CD8^+$ T cells, limiting PD-1-mediated immunosuppression, essential for a CTL activity against melanoma cells. The treatment using these mannosylated nano-vaccines undoubtedly increased the expression of the co-stimulatory OX40, which was then available at higher extent to be targeted by the immune checkpoint therapy.

Nevertheless, the levels of $CD8^+$ T cells within the tumour tend to decrease with time, while there was an increasing infiltration of Treg cells. As a consequence, the CD8:Treg ratio was low, indicating an immunosuppressive TME, which limits the expected antitumor immunity. In parallel, the levels of tumour infiltrated MDSC increased significantly in the TME, hampering infiltration of $CD8^+$ T cells and CTL activity [52,53]. Our mannosylated therapeutic nano-vaccines seem to induce infiltration

of MDSC into the TME over time. The infiltration of MDSC hindered the early effect of $CD8^+$ T cell stimulation and proliferation, inhibiting T cell infiltration and CTL activity in the TME. This imbalance promoted an immunosuppressive TME, and the combination of mannosylated nano-vaccines + αPD-1/αOX40 failed to show benefit in comparison with αPD-1/αOX40 alone.

Considering the high levels of MDSC, we hypothesized that the inhibition of these suppressor cells with ibrutinib, could remarkably improve the clinical outcomes of our strategy. Ibrutinib was shown to limit the generation and migration of MDSC, and was proposed as a strategy to enhance cancer immunotherapeutic strategies [20,54].

Our findings demonstrate that the mannosylated nano-vaccines + αPD-1/αOX40 + ibrutinib induced remarkable tumour remission and/or tumour growth inhibition in two tumor-bearing mouse models, with long-term survival. The αPD-1/αOX40 + ibrutinib contributed to a homeostasis in the TME ideal for antitumor vaccination. By depleting MDSC, ibrutinib revealed the full potential of our mannosylated nano-vaccines in enhancing T cell responses at the TME, rendering them to be available for immune checkpoint therapy with αPD-1 and αOX40. The addition of ibrutinib also improved DC maturation and $CD4^+$ T cell proliferation, increasing the secretion of cytokines essential for the expansion of $CD8^+$ T cells, while trafficking into the TME.

Of note, this strong therapeutic synergism of our nano-vaccines with ibrutinib and αPD-1/αOX40 immune checkpoint therapy was only obtained when the mannose moieties were grafted on the surface of the nano-vaccines. These data prove the superior impact of mannosylation of our NP in the DC-mediated antigen

presentation and the activation of tumour-antigen specific T cells in the melanoma therapeutic setting.

Taken together, although each of these components had modest results as monotherapy, their combination resulted in robust and widespread complementary outcomes. These results provide a strong basis to devise novel regimens and combination therapies for solid tumours, unravelling the full potential of particulate mannosylated cancer nano-vaccines.

References

1 Topalian, S. L. *et al.* Safety, Activity, and Immune Correlates of Anti–PD-1 Antibody in Cancer. *New England Journal of Medicine* **366**, 2443-2454, doi:doi:10.1056/NEJMoa1200690 (2012).

2 Hodi, F. S. *et al.* Improved survival with ipilimumab in patients with metastatic melanoma. *N Engl J Med* **363**, 711-723, doi:10.1056/NEJMoa1003466 (2010).

3 Gramaglia, I. *et al.* The OX40 costimulatory receptor determines the development of CD4 memory by regulating primary clonal expansion. *J Immunol* **165**, 3043-3050 (2000).

4 Arch, R. H. & Thompson, C. B. 4-1BB and Ox40 are members of a tumor necrosis factor (TNF)-nerve growth factor receptor subfamily that bind TNF receptor-associated factors and activate nuclear factor kappaB. *Mol Cell Biol* **18**, 558-565 (1998).

5 Aspeslagh, S. *et al.* Rationale for anti-OX40 cancer immunotherapy. *Eur J Cancer* **52**, 50-66, doi:10.1016/j.ejca.2015.08.021 (2016).

6 Sarff, M. *et al.* OX40 (CD134) expression in sentinel lymph nodes correlates with prognostic features of primary melanomas. *Am J Surg* **195**, 621-625; discussion 625, doi:10.1016/j.amjsurg.2007.12.036 (2008).

7 Vetto, J. T. *et al.* Presence of the T-cell activation marker OX-40 on tumor infiltrating lymphocytes and draining lymph node cells from patients with melanoma and head and neck cancers. *Am J Surg* **174**, 258-265 (1997).

8 Spranger, S. *et al.* Mechanism of tumor rejection with doublets of CTLA-4, PD-1/PD-L1, or IDO blockade involves restored IL-2 production and proliferation of CD8+ T cells directly within the tumor microenvironment. *Journal for ImmunoTherapy of Cancer* **2**, 3, doi:10.1186/2051-1426-2-3 (2014).

9 Gajewski, T. F. The Next Hurdle in Cancer Immunotherapy: Overcoming the Non-T-Cell-Inflamed Tumor Microenvironment. *Semin Oncol* **42**, 663-671, doi:10.1053/j.seminoncol.2015.05.011 (2015).

10 Minn, A. J. & Wherry, E. J. Combination Cancer Therapies with Immune Checkpoint Blockade: Convergence on Interferon Signaling. *Cell* **165**, 272-275, doi:10.1016/j.cell.2016.03.031 (2016).

11 Tumeh, P. C. *et al.* PD-1 blockade induces responses by inhibiting adaptive immune resistance. *Nature* **515**, 568-571, doi:10.1038/nature13954 (2014).

12 Kodumudi, K. N., Weber, A., Sarnaik, A. A. & Pilon-Thomas, S. Blockade of myeloid-derived suppressor cells after induction of lymphopenia improves adoptive T cell therapy in a murine model of melanoma. *J Immunol* **189**, 5147-5154, doi:10.4049/jimmunol.1200274 (2012).
13 Meyer, C. *et al.* Frequencies of circulating MDSC correlate with clinical outcome of melanoma patients treated with ipilimumab. *Cancer Immunol Immunother* **63**, 247-257, doi:10.1007/s00262-013-1508-5 (2014).
14 van Kooyk, Y. C-type lectins on dendritic cells: key modulators for the induction of immune responses. *Biochem Soc Trans* **36**, 1478-1481, doi:10.1042/BST0361478 (2008).
15 Silva, J. M. *et al.* In vivo delivery of peptides and Toll-like receptor ligands by mannose-functionalized polymeric nanoparticles induces prophylactic and therapeutic anti-tumor immune responses in a melanoma model. *J Control Release* **198**, 91-103, doi:10.1016/j.jconrel.2014.11.033 (2015).
16 Alonso-Sande, M. *et al.* Development of PLGA-Mannosamine Nanoparticles as Oral Protein Carriers. *Biomacromolecules* **14**, 4046-4052, doi:10.1021/bm401141u (2013).
17 Alonso-Sande, M. *et al.* Development of PLGA-mannosamine nanoparticles as oral protein carriers. *Biomacromolecules* **14**, 4046-4052, doi:10.1021/bm401141u (2013).
18 Garinot, M. *et al.* PEGylated PLGA-based nanoparticles targeting M cells for oral vaccination. *J Control Release* **120**, 195-204, doi:10.1016/j.jconrel.2007.04.021 (2007).
19 Wang, X., Ramstrom, O. & Yan, M. Dynamic light scattering as an efficient tool to study glyconanoparticle-lectin interactions. *Analyst* **136**, 4174-4178, doi:10.1039/c1an15469a (2011).
20 Stiff, A. *et al.* Myeloid-Derived Suppressor Cells Express Bruton's Tyrosine Kinase and Can Be Depleted in Tumor-Bearing Hosts by Ibrutinib Treatment. *Cancer Research* **76**, 2125-2136, doi:10.1158/0008-5472.Can-15-1490 (2016).
21 Natarajan, G. *et al.* A Tec kinase BTK inhibitor ibrutinib promotes maturation and activation of dendritic cells. *OncoImmunology* **5**, doi:10.1080/2162402x.2016.1151592 (2016).
22 Swart, M., Verbrugge, I. & Beltman, J. B. Combination Approaches with Immune-Checkpoint Blockade in Cancer Therapy. *Front Oncol* **6**, 233, doi:10.3389/fonc.2016.00233 (2016).
23 Guo, Z. *et al.* PD-1 blockade and OX40 triggering synergistically protects against tumor growth in a murine model of ovarian cancer. *PLoS One* **9**, e89350, doi:10.1371/journal.pone.0089350 (2014).
24 Woods, D. M., Ramakrishnan, R., Sodré, A. L., Berglund, A. & Weber, J. Abstract A067: PD-1 blockade enhances OX40 expression on regulatory T-cells and decreases suppressive function through induction of phospho-STAT3 signaling. *Cancer Immunology Research* **4**, A067-A067, doi:10.1158/2326-6066.imm2016-a067 (2016).
25 De Koker, S. *et al.* Engineering Polymer Hydrogel Nanoparticles for Lymph Node-Targeted Delivery. *Angew Chem Int Ed Engl* **55**, 1334-1339, doi:10.1002/anie.201508626 (2016).
26 Azzi, J. *et al.* Targeted Delivery of Immunomodulators to Lymph Nodes. *Cell Rep* **15**, 1202-1213, doi:10.1016/j.celrep.2016.04.007 (2016).
27 Zhu, Q. *et al.* Using 3 TLR ligands as a combination adjuvant induces qualitative changes in T cell responses needed for antiviral protection in mice. *J Clin Invest* **120**, 607-616, doi:10.1172/JCI39293 (2010).

28 Chen, L. & Flies, D. B. Molecular mechanisms of T cell co-stimulation and co-inhibition. *Nat Rev Immunol* **13**, 227-242, doi:10.1038/nri3405 (2013).
29 Fang, H. *et al.* TLR4 is essential for dendritic cell activation and anti-tumor T-cell response enhancement by DAMPs released from chemically stressed cancer cells. *Cellular & Molecular Immunology* **11**, 150-159, doi:10.1038/cmi.2013.59 (2013).
30 Beyersdorf, N., Kerkau, T. & Hunig, T. CD28 co-stimulation in T-cell homeostasis: a recent perspective. *Immunotargets Ther* **4**, 111-122, doi:10.2147/ITT.S61647 (2015).
31 Hanahan, D. & Coussens, L. M. Accessories to the crime: functions of cells recruited to the tumor microenvironment. *Cancer Cell* **21**, 309-322, doi:10.1016/j.ccr.2012.02.022 (2012).
32 Burkholder, B. *et al.* Tumor-induced perturbations of cytokines and immune cell networks. *Biochim Biophys Acta* **1845**, 182-201, doi:10.1016/j.bbcan.2014.01.004 (2014).
33 Sagiv-Barfi, I. *et al.* Eradication of spontaneous malignancy by local immunotherapy. *Sci Transl Med* **10**, doi:10.1126/scitranslmed.aan4488 (2018).
34 Seliger, B., Ruiz-Cabello, F. & Garrido, F. IFN inducibility of major histocompatibility antigens in tumors. *Adv Cancer Res* **101**, 249-276, doi:10.1016/S0065-230X(08)00407-7 (2008).
35 Dranoff, G. *et al.* Vaccination with irradiated tumor cells engineered to secrete murine granulocyte-macrophage colony-stimulating factor stimulates potent, specific, and long-lasting anti-tumor immunity. *Proc Natl Acad Sci U S A* **90**, 3539-3543 (1993).
36 Kowalczyk, D. W. *et al.* Vaccine-induced CD8+ T cells eliminate tumors by a two-staged attack. *Cancer Gene Ther* **10**, 870-878, doi:10.1038/sj.cgt.7700653 (2003).
37 Miller, M. D. & Krangel, M. S. The human cytokine I-309 is a monocyte chemoattractant. *Proc Natl Acad Sci U S A* **89**, 2950-2954 (1992).
38 Henry, C. J., Ornelles, D. A., Mitchell, L. M., Brzoza-Lewis, K. L. & Hiltbold, E. M. IL-12 produced by dendritic cells augments CD8+ T cell activation through the production of the chemokines CCL1 and CCL17. *J Immunol* **181**, 8576-8584 (2008).
39 Pasare, C. & Medzhitov, R. Toll-like receptors: balancing host resistance with immune tolerance. *Curr Opin Immunol* **15**, 677-682 (2003).
40 Scheller, J., Chalaris, A., Schmidt-Arras, D. & Rose-John, S. The pro- and anti-inflammatory properties of the cytokine interleukin-6. *Biochim Biophys Acta* **1813**, 878-888, doi:10.1016/j.bbamcr.2011.01.034 (2011).
41 Fridlender, Z. G. *et al.* CCL2 blockade augments cancer immunotherapy. *Cancer Res* **70**, 109-118, doi:10.1158/0008-5472.CAN-09-2326 (2010).
42 Tsui, P. *et al.* Generation, characterization and biological activity of CCL2 (MCP-1/JE) and CCL12 (MCP-5) specific antibodies. *Hum Antibodies* **16**, 117-125 (2007).
43 Phan, G. Q. *et al.* Immunization of patients with metastatic melanoma using both class I- and class II-restricted peptides from melanoma-associated antigens. *J Immunother* **26**, 349-356 (2003).
44 Slingluff, C. L., Jr. *et al.* A randomized phase II trial of multiepitope vaccination with melanoma peptides for cytotoxic T cells and helper T cells for patients with metastatic melanoma (E1602). *Clin Cancer Res* **19**, 4228-4238, doi:10.1158/1078-0432.CCR-13-0002 (2013).
45 Shedlock, D. J. & Shen, H. Requirement for CD4 T cell help in generating functional CD8 T cell memory. *Science* **300**, 337-339, doi:10.1126/science.1082305 (2003).
46 Pizzurro, G. A. & Barrio, M. M. Dendritic cell-based vaccine efficacy: aiming for hot spots. *Front Immunol* **6**, 91, doi:10.3389/fimmu.2015.00091 (2015).

47 Almog, N. *et al.* Transcriptional switch of dormant tumors to fast-growing angiogenic phenotype. *Cancer Res* **69**, 836-844, doi:10.1158/0008-5472.CAN-08-2590 (2009).
48 Satchi-Fainaro, R. *et al.* Prospective identification of glioblastoma cells generating dormant tumors. *PLoS One* **7**, e44395, doi:10.1371/journal.pone.0044395 (2012).
49 van den Eertwegh, A. J. *et al.* Combined immunotherapy with granulocyte-macrophage colony-stimulating factor-transduced allogeneic prostate cancer cells and ipilimumab in patients with metastatic castration-resistant prostate cancer: a phase 1 dose-escalation trial. *Lancet Oncol* **13**, 509-517, doi:10.1016/S1470-2045(12)70007-4 (2012).
50 Hodi, F. S. *et al.* Ipilimumab plus sargramostim vs ipilimumab alone for treatment of metastatic melanoma: a randomized clinical trial. *JAMA* **312**, 1744-1753, doi:10.1001/jama.2014.13943 (2014).
51 Kaiser, A. D. *et al.* Towards a commercial process for the manufacture of genetically modified T cells for therapy. *Cancer Gene Ther* **22**, 72-78, doi:10.1038/cgt.2014.78 (2015).
52 Gabrilovich, D. I. & Nagaraj, S. Myeloid-derived suppressor cells as regulators of the immune system. *Nat Rev Immunol* **9**, 162-174, doi:10.1038/nri2506 (2009).
53 Nagaraj, S., Schrum, A. G., Cho, H. I., Celis, E. & Gabrilovich, D. I. Mechanism of T cell tolerance induced by myeloid-derived suppressor cells. *J Immunol* **184**, 3106-3116, doi:10.4049/jimmunol.0902661 (2010).
54 Sagiv-Barfi, I. *et al.* Therapeutic antitumor immunity by checkpoint blockade is enhanced by ibrutinib, an inhibitor of both BTK and ITK. *Proceedings of the National Academy of Sciences* **112**, E966-E972, doi:10.1073/pnas.1500712112 (2015).

ACKNOWLEDGMENTS

MultiNano@MBM project was supported by The Israeli Ministry of Health, and The Fundação para a Ciência e Tecnologia-Ministério da Ciência, Tecnologia e Ensino Superior (FCT-MCTES), under the frame of EuroNanoMed-II (ENMed/0051/2016; HF, RS-F, SJ). RS-F thanks the European Research Council (ERC) under the European Union's Seventh Framework Programme / ERC Consolidator Grant Agreement n. [617445]- PolyDorm, THE ISRAEL SCIENCE FOUNDATION (Grants No. 918/14 and 1969/18), The Melanoma Research Alliance (the Saban Family Foundation–MRA Team Science Award to RS-F and NE), The Israel Cancer Association (ICA) and the Israel Cancer Research Fund (ICRF). JC, AIM, CP, EZ and LM are supported by the FCT-MCTES (Fellowships SFRH/BD/87150/2012, PD/BD/113959/2015, SFRH/BD/87591/2012, SFRH/BD/78480/2011, SFRH / BPD / 94111 / 2013, respectively). This project has

received funding from European Structural & Investment Funds through the COMPETE Programme and from National Funds through FCT under the Programme grant SAICTPAC/0019/2015 (HF). We thank Elvira Haimov and Boris Redko from the Blavatnik Center for Drug Discovery at the Tel Aviv University for their professional and technical assistance with the peptide synthesis.

AUTHOR CONTRIBUTIONS

R.S.F. and H.F. conceived and designed all experiments. (ongoing)

XXX and XXX. performed the experiments: G. H. analyzed the data: I. J. contributed materials/analysis tools: A. B. and E. F. co-wrote the paper.

The authors do not have any conflict of interests to declare.

DATA AVAILABILITY

The authors declare that the data supporting the findings of this study are available within the paper and its Supplementary Information. Additional data and source files are available from the corresponding authors (RSF, HF) upon reasonable request.

ADDITIONAL INFORMATION

“Supplementary information is available in the online version of the paper. Reprints and permission information is available online at www.nature.com/reprints. Correspondence and requests for materials should be addressed to RSF and HF.”

FIGURE CAPTIONS

Fig. 1. NP and Man-NP are potential delivery systems for vaccination. A. Schematic representation of mannose-PLGA/PLA nanoparticles (man-NP). **B.** TEM image of spherical man-NP. **C.** SEM image of spherical man-NP. **D.** AFM images of spherical man-NP, showing narrow size polydispersity. **E**. Particle internalization by DC determined by FACS. Non-treated cells and non-labeled NP were used as negative controls. Data are presented as mean ± SD, *N* = 4-6, from three independent experiments performed in triplicate. **F**. Confocal images of DC after 3 hours of incubation with NP (left) and man-NP (right). Z-stacks (top) and projections (bottom). (N = 3; n = 6). Scale bars = 50 μm. **G.** Percentage of NP internalization 17 hours after immunization with empty NP or antigen-loaded NP. man-NP (TPGS) were preferentially internalized by circulating DC in immunized C57BL/6J mice and increased the expression of the activation and maturation markers of these APC. **H.** Median florescence intensity (MFI) of activated DC that internalized NP, present in the lymph nodes (LN), 17 hours after immunization. Mean ± SD; *N* = 3, n = 3, where *N* denotes the number of independent experiments and n denotes the number of measurements per experiment. Statistics: Two-way ANOVA followed by Tukey Post-Hoc test (**G.**) or Bonferroni test (**H.**) $*P < 0.05$, $**P < 0.01$ and $***P < 0.001$.

Fig. 2. NP and man-NP vaccines induce splenocyte activation and *ex vivo* cytotoxicity against melanoma cells. A. Non-invasive intravital fluorescence imaging of C57BL/6J mouse 3 hours and 48 hours following hock immunization with NP (left) and man-NP (right). **B.** Organ biodistribution according to fluorescence signal (*N* = 4) with NP and man-NP. Data represent mean ± SD**. C.** Immunization scheme of C57BL/6J mice and *ex vivo* splenocyte cytotoxic activity timeline. **D.**

Secretion of IFN-γ, GM-CSF, TNF-α, IL-2, IL-6, CCL1/TCA-3, MIP-1β, MCP-5/CCL12 and TARC/CCL17 upon re-stimulation of splenocytes in culture. **E.** Cytotoxic activity of splenocytes harvested from immunized C57BL/6J mice, after incubation with Melan-A/MART-1 and CD28 in solution for 6 days. Data are presented as mean ± SEM (N = 6). * P < 0.05; *** P < 0.001. **F.** Images of RMS cells co-cultured with reactivated splenocytes from the group immunized with NP MHCI-ag and MHCII-ag (top) and the group immunized with man-NP MHCI-ag/man-NP MHCII-ag (bottom). Cell death was detected with an apoptosis reagent that couples to activated caspase-3/7 recognition motif and quantifies apoptosis (in green).

Fig. 3. Prophylactic nano-vaccines have synergistic effect with PD-1 blockade and OX40 activation, restricting melanoma growth and prolonging survival. A. Timeline of immunization, tumor inoculation and immune checkpoint therapy. **B.** Tumor growth curve. P values correspond to tumor volume at day 17. Data are presented as mean ± SEM (N=4-5). **C.** Kaplan-Meier overall survival over time graph, for mice inoculated with 4.5 x 10^5 RMS cells (N = 4-5). **D.** Individual tumor volume at day 17 and **E.** Day 27 following tumor inoculation.

Fig. 4. Low $CD8^+$/Treg ratio and high infiltration of Myeloid-derived Suppressor Cells ($CD11b^+Gr\text{-}1^+$MDSC) compromise the therapeutic efficacy of the combination of mannosylated nano-vaccines with αPD-1/αOX40. A. Timeline of tumor inoculation and treatments. **B.** Tumor growth curve. Data are presented as mean ± SEM (N = 7). P values correspond to tumor volume at day 18 after tumor inoculation. **C.-H.** Tumor-infiltrating immune cell populations. Tumors were isolated on day 18 after tumor cell inoculation ($N \geq 3$) and when the tumor volume for final

endpoint was reached. Quantification was performed by flow cytometry. Data are presented as mean ± SD of 3 independent replicates. * $P < 0.05$; ** $P < 0.01$; *** $P < 0.001$.

Fig. 5. Trivalent combination of mannosylated nano-vaccines with ibrutinib and αPD-1/αOX40 strongly restricts melanoma growth, leading to long-term survival. A. Timeline of tumor inoculation and treatments. **B.** Tumor growth curve. Data are presented as mean ± SEM ($N = 7$). *P* values correspond to tumor volume at day 20 after tumor inoculation. **C.** Percent of EGSRNQDWL (gp100)-specific $CD8^+$ T cells in the lymph nodes (LN). **D.** ELISpot representative images of IFN-γ spot forming cells among splenocytes after *ex vivo* re-stimulation with melan-A/MART-1 peptides on day 22. **E.** Kaplan-Meier overall survival over time graph, for mice inoculated with 3×10^5 RMS ($N = 13$-15). **F.** Individual tumor volume at days 27, 36 and 43 after tumor inoculation, with mean ± SEM represented (N=13-15). All data are presented as mean of 3 independent replicates. * $P < 0.05$; ** $P < 0.01$; *** $P < 0.001$.

Fig. 6. High $CD8^+$/Treg ratio and inhibition of MDSC are associated with improved therapeutic efficacy. A.-H. Tumor-infiltrating immune cell populations. Tumors were isolated on the first endpoint, day 20 after tumor cell inoculation ($N \geq 3$), and at the tumor size-matched second endpoint: day 27 for PBS, ibrutinib only and nano-vaccines + ibrutinib; day 35 for αPD-1/αOX40 + ibrutinib and nano-vaccines + αPD-1/αOX40. Quantification was performed by flow cytometry. Data are presented as mean ± SD of 3 independent replicates. * $P < 0.05$; ** $P < 0.01$; *** $P < 0.001$.

METHODS 3019 words

MATERIALS AND METHODS

Materials

Poly(L-lactic acid) (PLA, 2000 Da) with an average molecular weight (Mw) of 2000 was purchased from PolySciences, Inc., UK. Tumour-associated peptides MHCI-restricted Melan-A:26-35(L27), ELAGIGILTV, (MHCI-ag), and MHCII-restricted Melan-A:51-73(RR-23), RNGYRALMDKSLHVGTQCALTRR (MHCII-ag) were purchased to GeneCust Europe. Alternatively, the synthesis and purification of these Melan-A peptides was performed by the Blavatnik Center for Drug Discovery at the Tel Aviv University. The synthesis and purification of the gp100 peptides (MHCI-restricted gp100:25-33 (EGSRNQDWL) and MHCII-restricted gp100:44-59 (WNRQLYPEWTEAQRLD) was performed by the Blavatnik Center for Drug Discovery at Tel Aviv University. H-2D^{b}-restricted EGSRNQDWL PE-labelled tetramer was supplied by Quimigen S.L. (Madrid, Spain). CpG ODN 1826 (TCCATGACGTTCCTGACGTT) was purchased from InvivoGen (San Diego, CA, USA). MEM α, nucleosides, ascorbic acid was purchased from Invitrogen. RPMI 1640, heat inactivated foetal bovine serum (FBS), trypsin EDTA 0.05%, penicillin (10,000 Unit/ml) and streptomycin (10,000 μg/ml), sodium pyruvate (100 mM), GM-CSF recombinant mouse protein (5 ng/ml), HEPES buffer (1 M), ACK lysing buffer, paraformaldehyde (PFA) 4% (v/v), Wheat Germ Agglutinin (WGA), Alexa Fluor® 633 Conjugate, Hoechst® 33342 and AlamarBlue® reagent were purchased from Thermo Fisher Scientific. Proteome Profiler Mouse XL Cytokine Array Kit was purchased from R&D Systems, Inc. (Minneapolis, MN, USA). Matrigel Matrix (Cat. no. 356231) was

purchased from BD Biosciences - Discovery Labware, Erembodegem, Europe. IncuCyte® Caspase-3/7 Apoptosis Assay Reagent was acquired from Biological Industries Israel Beit-Haemek Ltd. PLGA (Resomer 503H; Mw 24 000 – 38 000), mannosamine·HCl, dimtehylformamide, 4-dimethylaminopyridine , *N*,*N*'-Dicyclohexylcarbodiimide, methanol, anhydrous sodium sulphate, Concanavalin A, FITC-labelled Concanavalin A from Canavalia ensiformis (Jack bean) Type IV lyophilized powder, Lipid A monophosphoryl from *Salmonella enterica* serotype minnesota Re 595 (Re mutant) (MPLA), bovine serum albumin, d-α-tocopherol polyethylene glycol 1000 succinate (TPGS), Poly(vinyl alcohol) (PVA) Mw 13,000 to 23,000 Da, 99% hydrolysed, dichloromethane (DCM) and chloroform-d were purchased from Sigma Aldrich. PD-1 and OX40 monoclonal antibodies were acquired from Bio X cell. Rabbit monoclonal anti-caspase 3 was purchased from Epitomics (CA, USA). Antibodies anti-mouse CD4 (clone: CK1.5), CD8α (clone: 53-6.7) and DAPI were acquired from BioLegend (San Diego, CA, USA). Streptavidin−horseradish peroxidase conjugate was purchased from Histostain, Life Technologies (CA, USA). Fluorochrome labelled antibodies for flow cytometry were purchased from Miltenyi Biotech, unless otherwise specified. ELISpot kit was purchased by R&D Systems Inc. (Minneapolis, USA).

Synthesis and characterization of mannose-PLGA polymer

Mannose-PLGA (man-PLGA) was synthesized from PLGA (Resomer 503H; Mw 24,000 – 38,000 Da). Carboxylic acid terminal groups of PLGA were modified with mannosamine under nitrogen atmosphere in mild conditions [17]. Briefly, Mannosamine·HCl (10.8 mg, 0.05 mmol, 3.5 eq.) and 4-dimethylaminopyridine (6.5

mg, 0.05 mmol, 4 eq.) were added to 4 ml of dimethylformamide. The mixture was stirred for 10 minutes at room temperature to achieve complete dissolution of mannosamine. PLGA (Resomer 503H; Mw 24 000 – 38 000) (400 mg, 0.0133 mmol, 1 eq.) was added to the previous solution and stirred for 10 minutes at room temperature. *N*,*N*'-Dicyclohexylcarbodiimide (5.5 mg, 0.027 mmol, 2 eq.) was added to induce the reaction between PLGA and mannosamine. The reaction was allowed to stir for 48 hours at room temperature under argon atmosphere. The polymer was precipitated with water and recovered by centrifugation. Man-PLGA was dissolved in DCM and dried over anhydrous sodium sulphate. The solution was filtered. DCM was evaporated through rotary evaporation. Methanol was added to precipitate the polymer and wash the reaction crude. Man-PLGA was dissolved in DCM and the precipitation was repeated. Finally, man-PLGA was dried under vacuum overnight and weighed after 24 hours (186.7 mg; η = 47%).

Nuclear Magnetic resonance

Details are described in the Supplementary Methods.

Synthesis of NP and man-NP

PLGA/PLA NP were formulated by the double emulsion-solvent evaporation (w/o/w) method [18]. PLGA/PLA (2:8) blend was dissolved in dichloromethane (DCM) at 50 mg/ml. MPLA (100 µg) was added to DCM polymer solution. A 10% (m/v) PVA aqueous solution (100 µl) containing CpG at 0.5 mg/ml and melan-A/MART-1 (26-35(A27L), melan-A/MART-1 (51-73), gp100 (25-33) or gp100 (44-59) at 5 mg/ml was added to DCM. For empty NP, 100 µl of 10% PVA aqueous solution was added. The mixture was emulsified with a microprobe ultrasonic processor for 15 seconds at 20%

amplitude. TPGS aqueous solution 2.5% (m/v) (400 µl) was added and the second emulsion was formed using the same conditions. The double emulsion was added dropwise into a 0.25% (m/v) PVA aqueous solution and stirred for 1 hour at room temperature. Particle suspension was collected by centrifugation at 20,000 *g* for 45 minutes, 4ºC (SORVALL® RC-5B PLUS Superspeed centrifuge). Particles were washed with ultrapure water, collected by centrifugation and finally resuspended in PBS or ultrapure water. Mannose-PLGA/PLA nanoparticles (man-NP) were prepared as previously described with man-PLGA/PLA (2:8) blend instead. Cy5.5-labeled NP and man-NP were synthesized by adding 0.5 µg to the polymer blend.

Size Distribution and ζ-Potential Measurements

Particle size was measured by Dynamic Light Scattering with Malvern Nano ZS (Malvern Instruments, UK). Z-average size was determined by cumulative analysis. ζ-Potential of particles was measured by Laser Doppler Velocimetry in combination with Phase Analysis Light Scattering with the same equipment. Particles were diluted in ultrapure water and electrophoretic mobility was determined at 25°C with the Helmholtz-von Smoluchowski model.

Particle morphology

Atomic Force Microscopy (AFM). Particles were diluted at 5 mg/ml in ultrapure water. A drop of sample was placed onto freshly cleaved mica for 20 minutes and dried with pure N_2. Samples were analysed by AFM in tapping mode in air at room temperature, using a Nanoscope IIIa Multimode Atomic Force Microscope (Digital Instruments, Veeco), and etched silicon tips (ca. 300 kHz), at a scan rate of ca. 1.6 Hz.

Scanning Electron Microscopy (SEM). Particles were diluted in trehalose 5% (m/v) and fast frozen at -80ºC for 2 hours. Samples were dried under vacuum, first at -20ºC for 14 hours and then at 20ºC for 2 hours. Dried specimens were coated with gold on a Peltier-cold stage sputter-coater and examined using a FEI Quanta 200 FEG ESEM Phillips 500 scanning electron microscope at 5 kV accelerating voltage.

Transmission Electron Microscopy. Particles were diluted in PBS and placed on a carbon-coated copper grid and dried. Samples were analysed by Philips CM 120 Bio-Twin TEM.

Entrapment efficiency and loading capacity of antigens and immune potentiators

Supernatants collected from centrifugations were used for indirect quantification of entrapped antigens and immune potentiators. Entrapment efficiency (EE % (m/m), Eq. (1)) and loading capacity (LC µg/mg, Eq. (2)) of melan-A/MART-1 (26-35(A27L)) and melan-A/MART-1 (51-73) were determined with FAM-labelled melan-A/MART-1 (26-35(A27L)) and melan-A/MART-1 (51-73), respectively. Relative Fluorescence Units (RFU) were measured with SpectraMax M5e plate reader (Molecular Devices, CA, USA) at 498/518 nm, excitation/emission wavelengths. The amount of CpG in the supernatant was determined by the Oligreen® ssDNA quantitation kit [15]. RFU were measured using the fluorometer at 485 nm excitation and 530 nm emission wavelengths.

$$Entrapment\ Efficiency\ (EE\ \%) = \frac{initial\ amount\ of\ agent - amount\ of\ agent\ in\ the\ supernatant}{initial\ amount\ of\ agent} \times 100 \quad (1)$$

$$Loading\ Capacity\ (LC\ \mu g/mg) = \frac{initial\ amount\ of\ agent - amount\ of\ agent\ in\ the\ supernatant}{total\ amount\ of\ polymer} \quad (2)$$

Mannose detection on the particles' surface by the Lectin Recognition Assay

Details are described in the Supplementary Methods.

Cell lines

Details are described in the Supplementary Methods.

***In vitro* cell viability in the presence of NP or man-NP**

Details are described in the Supplementary Methods.

Hemolysis assay

Details are described in the Supplementary Methods.

***In vitro* particle internalization by dendritic cells**

JAW SII DC ($5x10^4$ cells/well) were seeded in 96-well plates and incubated overnight. Cells were then incubated with rhodamine-grafted NP or man-NP (500 µg/ml) for 4, 12 and 24 hours. Cells were then washed with DPBS and resuspended in flow cytometry buffer. Non-treated cells and non-labelled NP were used as negative controls. An excess of soluble mannose (5 mM) was added to the medium, as a control, in order to confirm its ability to compete with man-NP for CD206 at DC surface. The individual fluorescence JAW SII DC was collected for each sample using LSR Fortessa cytometer (BD Biosciences) by Facs Diva, and analysed with FlowJo software version 7.6.5 for Microsoft (TreeStar, San Carlos, CA).

The 8-well Ibidi® µ-Slide microscopy chambers were incubated with 300 µL fibronectin (10 µg/mL) per well during 30 min in a humidified incubator with 5% CO_2, at 37°C. After discarding the volume of fibronectin, JAW SII cells ($5x10^4$ cells/well)

were seeded in 8-well Ibidi® µ-Slide microscopy chambers for 6 hours in a humidified incubator with 5% CO_2, at 37°C. Cells were incubated with rhodamine-grafted NP or man-NP (500 µg/ml) for 3 hours. Non-treated cells and non-labelled NP were used as negative controls. Cells were washed and fixed at room temperature in 4% paraformaldehyde, containing Hoechst®332 at 2 µg/mL and WGA Alexa Fluor 633 at 5 µg/mL to stain the nucleus and the cell membrane, respectively. Each well was washed three times with PBS and 100 µL of fluoromount were added to each one. Particle internalization was observed by confocal microscopy using Zeiss LSM 710 with 63x amplification in oil. Images were processed with ImageJ software. Three-dimensional (3D) projection images were obtained from 0.4 µm Z-stacks and processed using the Leica Application Suite-Advanced Fluorescence (LAS-AF) software.

Animal studies

All animal procedures were performed in compliance with Tel Aviv University, Sackler Faculty of Medicine guidelines and with the Portuguese competent authority for animal protection, Direcção Geral de Alimentação e Veterinária, Lisbon, Portugal. The protocols were approved by the institutional animal care and use committee (IACUC) and performed in accordance with NIH guidelines.

Male C57BL/6J mice (8 weeks old) were purchased from Envigo LTD (Jerusalem, Israel) or Charles River (Écully, France), and housed in the animal facility of Tel Aviv University or at the Faculty of Pharmacy, University of Lisbon. The number of animals in each group was determined according to previous studies (*26, 58*).

Mice body weight change was monitored 3 times per week. Mice were euthanized according to ethical protocol when showing signs of distress or with rapid

weight loss (above 10% within a few days or 20% from the initial weight). Tumour-bearing mice were euthanized in case the tumour size exceeded 2000 mm^3 or if the tumour was necrotic or ulcerative. Mice were perfused intracardially with PBS, immediately after euthanasia, tumours were dissected and incubated in 4% PFA and collected for histology.

***In vivo* study of man-NP internalization by DC in draining lymph nodes**

Male C57BL/6, 8 weeks old mice (n = 3 / group) were injected into the right flank by the s.c. hock immunization with one of the Cy5.5 fluorescently-labelled plain and antigen-loaded NP formulations (2 mg of NP/mouse). Left non-injected flank served as negative control. All formulations contained MART-1 antigens and TLR ligands. Popliteal and inguinal lymph nodes were harvested 16 h post-immunization (p.i.). A single-cell suspension was stained with fluorescent-labelled anti-mouse antibodies against CD11c, MHCII (I-Ab), MHCI (H-2Kb), CD80 and CD86, for 20 min at 4ºC. Samples were acquired with an LSR II Fortessa flow cytometer (BD Bioscience) and analysed with FlowJo software (Treestar).

Immunization of animals with tumour-associated antigens

For immunization studies, 8 weeks old C57BL/6J male mice were randomized into 8 groups (*N* = 6) (**Supplementary Table 1**).

Treatments (100 µl) were injected into each mouse by hock immunization, via s.c. injection proximal to popliteal LN. Half dose was injected into the right side and the other half into the left side. When the two peptide antigens melan-A/MART-1 (26-35(A27L)) and melan-A/MART-1 (51-73) were administered to the same mouse (groups 4, 6, and 8), 25 µl of each treatment was administered on each side. Each

dose contained 100 µg of antigen (50 µg of melan-A/MART-1 (26-35(A27L)) and 50 µg of melan-A/MART-1 (51-73), when two antigens were used), plus 20 µg of CpG and 20 µg of MPLA, either free in solution or entrapped in 2 mg of particles (20 mg/ml).

Tumour antigen specific-proliferation of splenocytes from immunized mice

Splenocytes from whole spleens of treated C57BL/6J mice (*N* = 6) were harvested and seeded in sterile 60 mm petri dishes, 10 days after the last immunization. Splenocytes were seeded for 6 days in complete RPMI medium, in the presence of melan-A/MART-1 (26-35(A27L)) or melan-A/MART-1 (26-35(A27L)) + melan-A/MART-1 (51-73) (0.1 mg/ml) (for groups 4, 6, and 8) and CD28 (2 µg/ml).

Splenocyte cytokine and chemokine secretion from immunized mice

A membrane-based sandwich immunoassay was performed according to the manufacturer protocol of Proteome Profiler Mouse Cytokine Array Panel A Kit (catalogue number: R&D-ARY0068; R&D Systems Inc., Minneapolis, USA). Splenocyte's culture media from each group (**Supplementary Table 1**) were pooled (n = 6) and concentrated in concentration tubes (Amicon). Each sample was applied on a nitrocellulose membrane containing capture antibodies that bind to specific target protein. After overnight incubation at 4ºC, streptavidin-HRP and chemiluminescent reagents were added, and incubation steps were performed according to the protocol provided by the analysis kit. Membranes were exposed to X-rays for 10 minutes. Results were detected by a transmission-mode scanner proportionally to the quantity of analyte and determined by protein array analyser software.

Ex vivo immune cell killing assay

Immune cell cytotoxic activity was assessed using IncuCyte® ZOOM live-cell instrument. RMS cells (6x10^3 cells/well) were seeded in 96-well plates in complete RMPI without phenol red, on the day before the addition of splenocytes. Pre-stimulated splenocytes were added to RMS cells in a 1:100 ratio. IncuCyte™ Caspase-3/7 Apoptosis Assay Reagent was diluted in RPMI without phenol red and added to each well to final concentration of 5 µM. Data was collected every 2 hours for 12 hours. Triton X-100 0.5% (v/v) and cell culture medium were used as positive and negative controls, respectively.

Tumour inoculation, combination therapies, and tumour volume measurements

Male C57BL/6J mice (8 weeks old) were randomized into different groups (*N* = 4-5) according to **Supplementary Table 2** for the prophylactic combination study. Different schedules were used for the prophylactic (**Fig. 3A**) and intervention combinatorial studies without or with the addition of ibrutinib (**Fig. 4A** and **Fig. 5A**, respectively). For the prophylactic study, on day 0, 50 µl of cell suspension containing 4.5x10^5 murine RMS cells mixed with growth-factor reduced matrigel (1:1) were inoculated subdermally on the right dorsal region as reported before [55]. For the intervention studies, the amount of murine RMS and Ret cells that were inoculated on day 0 was 3x10^5 instead. For the intervention study on the second melanoma model, 100 µl of saline with 1.5x10^5 B16-F10 cells in suspension were inoculated subdermally in the right flank. For both tumour models, mice were anesthetized with ketamine (100 mg/kg) and xylazine (12 mg/kg). The right dorsal area was treated with depilatory cream before the injection. αPD-1 and αOX40 were administered

intraperitoneally at 10 mg/kg. Ibrutinib was also administered intraperitoneally at 6 mg/kg. Tumour size was measured every 3 days with a calliper. Tumour volume was determined by $X^2 \cdot Y \cdot 0.5$ (X – small diameter; Y – large diameter) and body weight was monitored twice a week.

Immunohistochemistry

Details are described in the Supplementary Methods.

Flow cytometric analysis of tumour-infiltrated immune populations

RMS tumours were isolated from the animals directly after euthanasia. Tumour single-cell suspensions were obtained by mechanical disruption of the tissues and enzymatic digestion in RMPI medium with 0.5% BSA, 0.1% collagenase type II (LS004177, Worington), 0.1% dispase (LS02109, Worthington) and DNase (LS002007, Worington) for 1 hour at 37ºC. After digestion, the suspension was filtered through a 70 μm filter (BD Biosciences) to remove the debris. For the RMS cells, the obtained single-cell suspension was then stained with fluorochrome labelled antibodies and analysed using an LSR Fortessa (BD Biosciences) and FlowJo software (Tree Star Inc.). Intracellular staining was performed with the Inside stain kit (Miltenyi Biotec, Cat.# 130-090-477), according to the manufacturer's protocol. Details of the anitbodies used in each panel are in Supplementary information.

Functional assessment of T-cells

For the ELISpot assay, on day 0, 50 µl of cell suspension containing 4.5×10^5 murine RMS cells were inoculated subdermally. Starting on day 7, mice were treated with two weekly doses as reported in **Supplementary Table 3.**

On day 21, mice were euthanised and spleens harvested and splenocytes isolated. Splenocytes were seeded at $2x10^5$ cells per well in 96-well plates coated with IFN-γ antibody (R&D Systems Inc.) and incubated for 20 hours with 1 mg/mL of Melan-A/MART-1 MHCI-ag peptide. The secreted and captured IFN-γ was subsequently detected using a biotinylated antibody specific for IFN-γ and an alkaline-phosphatase conjugated to streptavidin. Following the addition of substrate solution, a blue coloured precipitate forms and appears as spots at the sites of cytokine localization. Automated spot quantification was performed using a UV ImmunoSpot® S6 Ultra-V.

For the tetramer staining assay, male C57BL/6J, 8-week-old mice were s.c. immunized into both right and left inguinal area, 2 times, once a week, with 100 µL of man-NP or NP (100 µg of gp 100 antigens/20 µg of CpG/20 µg of MPLA per mouse; 50 µL in each side), free gp 100 antigens with adjuvants CpG and MPLA, or PBS. Inguinal LN were harvested 10 days after the 2^{nd} injection, homogenized in a single-cell suspension, and plated in 96-well plate for staining. First, the peptide-MHC tetramer tagged with PE (H-$2D^b$ – restricted EGSRNQDWL PE-labelled tetramer (Quimigen S.L., Madrid, Spain)) was added to the single cell suspension, including FcR blocking, following supplier instructions. After 30 min of incubation at 4ºC, the cells were washed to remove unbound tetramers, and centrifuged at 1300 rpm, for 10 min, 10ºC. Cells were resuspended in ice-cold sorter buffer and plated in 96-well plates. After adding a mix of the antibodies CD3-APC-Cy7 and CD8α-PE-Cy7, cells were incubated for 15 min, at 4ºC protected from light. Cells were washed, centrifuged and resuspended in 200 µl of ice-cold sorter buffer to determine the percentages of tumour antigen-specific $CD3^+$ $CD8\alpha^+$ T cells by FACS.

Statistical Methods

Data are presented as mean ± standard deviation (SD) for *in vitro* assays and as mean ± standard error of the mean (SEM) for *ex vivo* and *in vivo* assays. Statistical analyses were performed with Student's t-test and one-way analysis of variance (ANOVA), followed by Bonferroni post hoc test for comparison of multiple groups with IBM SPSS® Statistics (Version 21, Microsoft). Statistical significance in overall survival was determined with log-rank test using SigmaPlot software (Systat Software Inc.) and GraphPad Prism 5® or 7® (GraphPad Software, Inc., La Jolla, CA) $P < 0.05$ was considered statistically significant.

Table 1. Particle size, polydispersity index (PdI) and ζ-Potential

Particles[d]	Size[a] (nm ± SD[b])	PdI[c] ± SD[b]	ζ-Potential (mV ± SD[b])
NP (empty)	168 ± 10	0.15 ± 0.05	-2.17 ± 0.40
NP MHCI-ag	178 ± 6	0.16 ± 0.03	-3.11 ±0.50
NP MHCII-ag	170 ± 5	0.18 ± 0.03	-2.34 ± 0.65
man-NP (empty)	169 ± 16	0.13 ± 0.05	-2.11 ± 0.40
man-NP MHCI-ag	181 ± 8	0.15 ± 0.04	-3.02 ± 0.46
man-NP MHCII-ag	166 ± 5	0.18 ± 0.04	-1.72 ± 0.47

[a] Z-average hydrodynamic diameter.

[b] SD, standard deviation.

[c] PdI, polydispersity index.

[d] CpG and MPLA were entrapped in all NP and man-NP, with exception of empty nanoparticulate systems.

For each formulation, we prepared 5 batches (N = 5) and measured in triplicate (n = 3).

Table 2. Entrapment Efficiency (EE) and Loading Capacity (LC) of antigens in NP and man-NP

Particles	EE (% ± SD[a])	LC (μg/mg ± SD[a])
NP MHCI-ag	99.1 ± 0.1	49.6 ± 0.05
NP MHCII-ag	82.4 ± 0.6	41.2 ± 0.3
man-NP MHCI-ag	97.5 ± 0.2	48.8 ± 0.1
man-NP MHCII-ag	74.6 ± 3.5	37.3 ± 1.7

[a] SD, standard deviation.

For each formulation, we prepared 4 batches (N = 4) and measured in triplicate (n = 3).

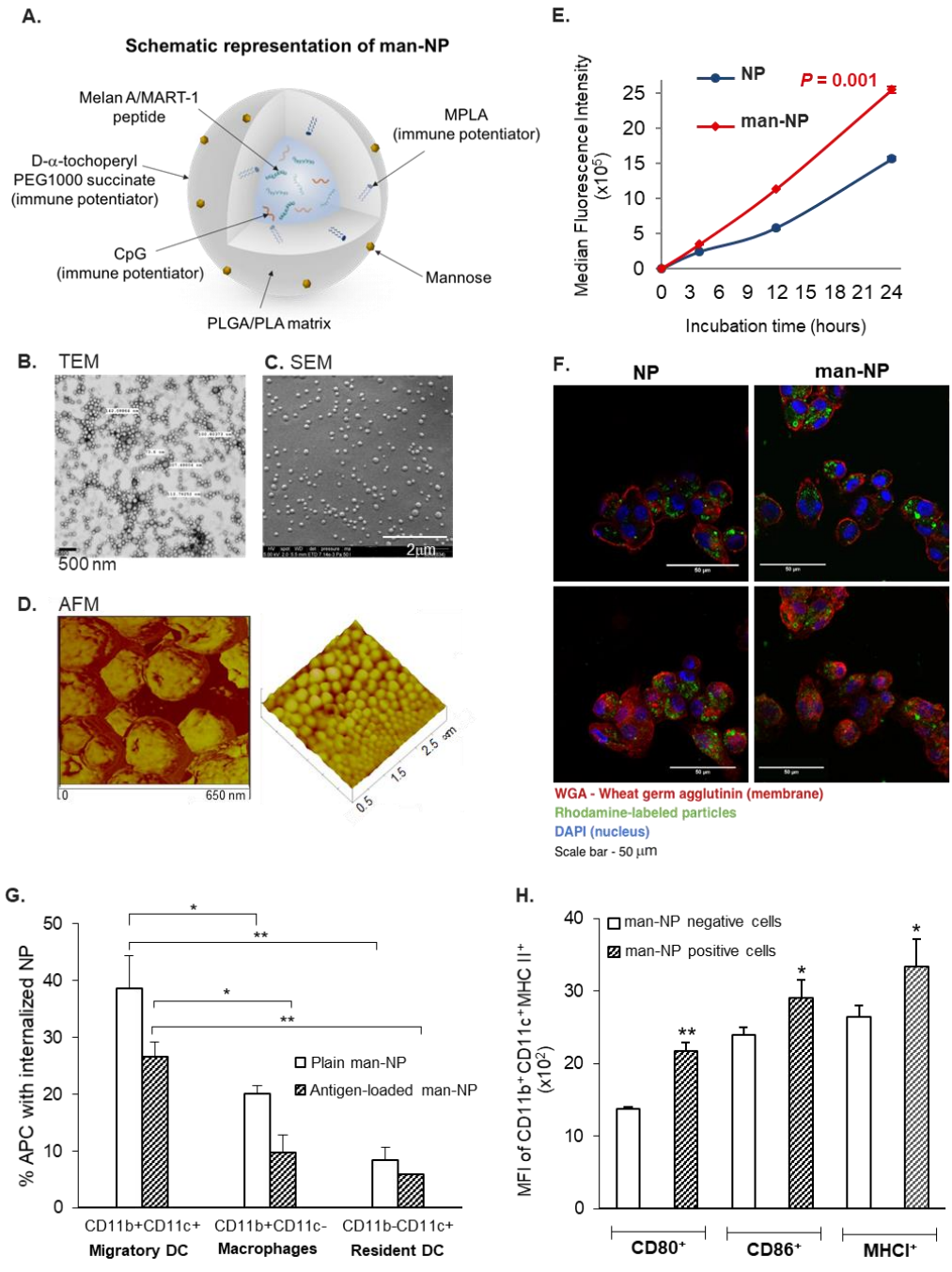

Fig. 1. NP and Man-NP are potential delivery systems for vaccination. A. Schematic representation of mannose-PLGA/PLA nanoparticles (man-NP). **B.** TEM image of spherical man-NP. **C.** SEM image of spherical man-NP. **D.** AFM images of spherical man-NP, showing narrow size polydispersity. **E**. Particle internalization by DC determined by FACS. Non-treated cells and non-labelled NP were used as negative controls. Data are presented as mean ± SD, *N* = 4-6, from three independent

experiments performed in triplicate. **F**. Confocal images of DC after 3 hours of incubation with NP (left) and man-NP (right). Z-stacks (top) and projections (bottom). (N = 3; n = 6). Scale bars = 50 μm. **G.** Percentage of NP internalization 17 hours after immunization with empty NP or antigen-loaded NP. man-NP (TPGS) were preferentially internalized by circulating DC in immunized C57BL/6J mice and increased the expression of the activation and maturation markers of these APC. **H.** Median florescence intensity (MFI) of activated DC that internalized NP, present in the lymph nodes (LN), 17 hours after immunization. Mean ± SD; *N* = 3, n = 3, where *N* denotes the number of independent experiments and n denotes the number of measurements per experiment. Statistics: Two-way ANOVA followed by Tukey Post-Hoc test (**G.**) or Bonferroni test (**H.**) *$P < 0.05$, **$P < 0.01$ and ***$P < 0.001$.

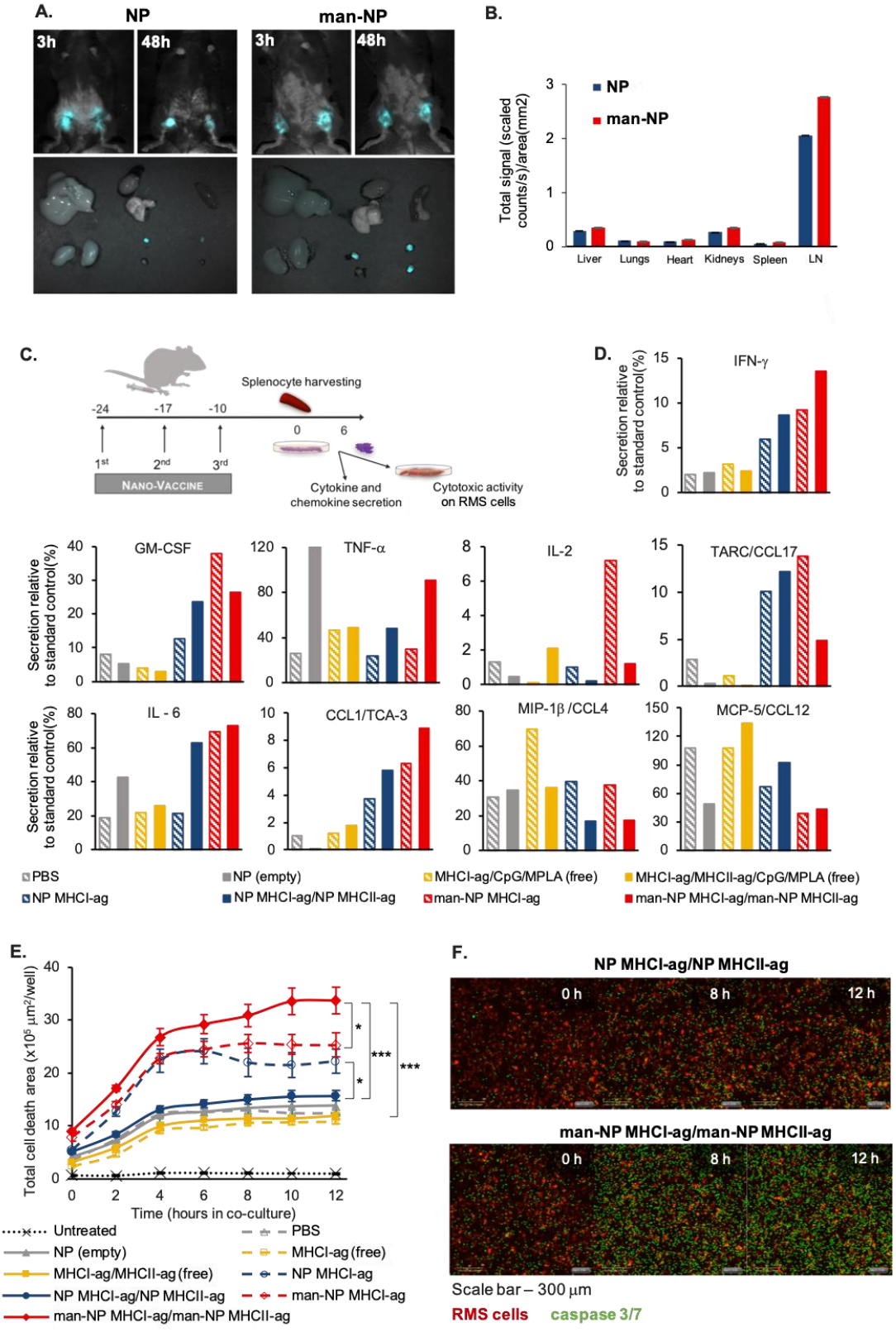

Fig. 2. NP and man-NP vaccines induce splenocyte activation and *ex vivo* cytotoxicity against melanoma cells. A. Non-invasive intravital fluorescence

imaging of C57BL/6J mouse 3 hours and 48 hours following hock immunization with NP (left) and man-NP (right). **B.** Organ biodistribution according to fluorescence signal (*N* = 4) with NP and man-NP. Data represent mean ± SD**. C.** Immunization scheme of C57BL/6J mice and *ex vivo* splenocyte cytotoxic activity timeline. **D.** Secretion of IFN-γ, GM-CSF, TNF-α, IL-2, IL-6, CCL1/TCA-3, MIP-1β, MCP-5/CCL12 and TARC/CCL17 upon re-stimulation of splenocytes in culture. **E.** Cytotoxic activity of splenocytes harvested from immunized C57BL/6J mice, after incubation with Melan-A/MART-1 and CD28 in solution for 6 days. Data are presented as mean ± SEM (*N* = 6). * $P < 0.05$; *** $P < 0.001$. **F.** Images of RMS cells co-cultured with reactivated splenocytes from the group immunized with NP MHCI-ag and MHCII-ag (top) and the group immunized with man-NP MHCI-ag/man-NP MHCII-ag (bottom). Cell death was detected with an apoptosis reagent that couples to activated caspase-3/7 recognition motif and quantifies apoptosis (in green).

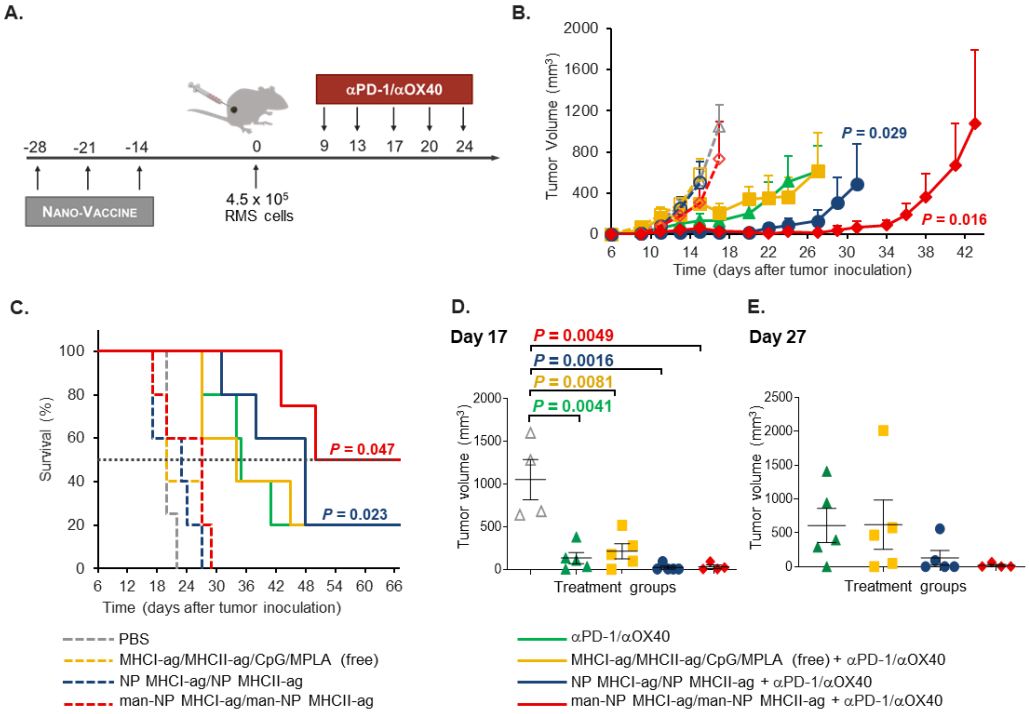

Fig. 3. Prophylactic nano-vaccines have synergistic effect with PD-1 blockade and OX40 activation, restricting melanoma growth and prolonging survival. A. Timeline of immunization, tumour inoculation and immune checkpoint therapy. **B.** Tumour growth curve. *P* values correspond to tumour volume at day 17. Data are presented as mean ± SEM (*N*=4-5). **C.** Kaplan-Meier overall survival over time graph, for mice inoculated with 4.5 x 10^5 RMS cells (*N* = 4-5). **D.** Individual tumour volume at day 17 and **E.** Day 27 following tumour inoculation.

endpoint and, therefore, corroborates higher tumour growth rate.

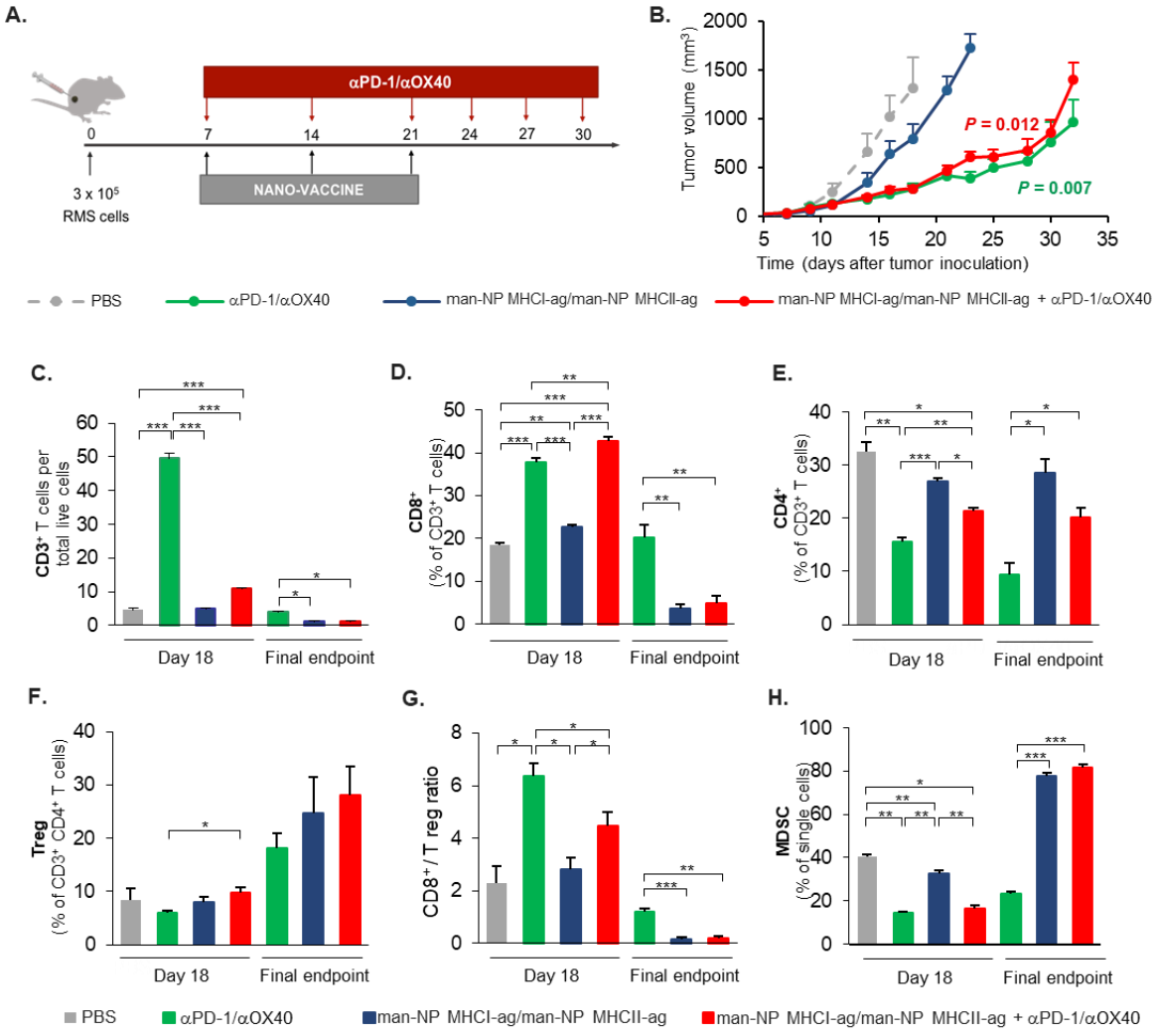

Fig. 4. Low CD8⁺/Treg ratio and high infiltration of Myeloid-derived Suppressor Cells (CD11b⁺Gr-1⁺MDSC) compromise the therapeutic efficacy of the combination of mannosylated nano-vaccines with αPD-1/αOX40. A. Timeline of tumor inoculation and treatments. **B.** Tumour growth curve. Data are presented as mean ± SEM (N = 7). P values correspond to tumour volume at day 18 after tumour inoculation. **C.-H.** Tumour-infiltrating immune cell populations. Tumours were isolated on day 18 after tumour cell inoculation ($N \geq 3$) and when the tumour volume for final endpoint was reached. Quantification was performed by flow cytometry. Data are

presented as mean ± SD of 3 independent replicates. * $P < 0.05$; ** $P < 0.01$; *** $P < 0.001$.

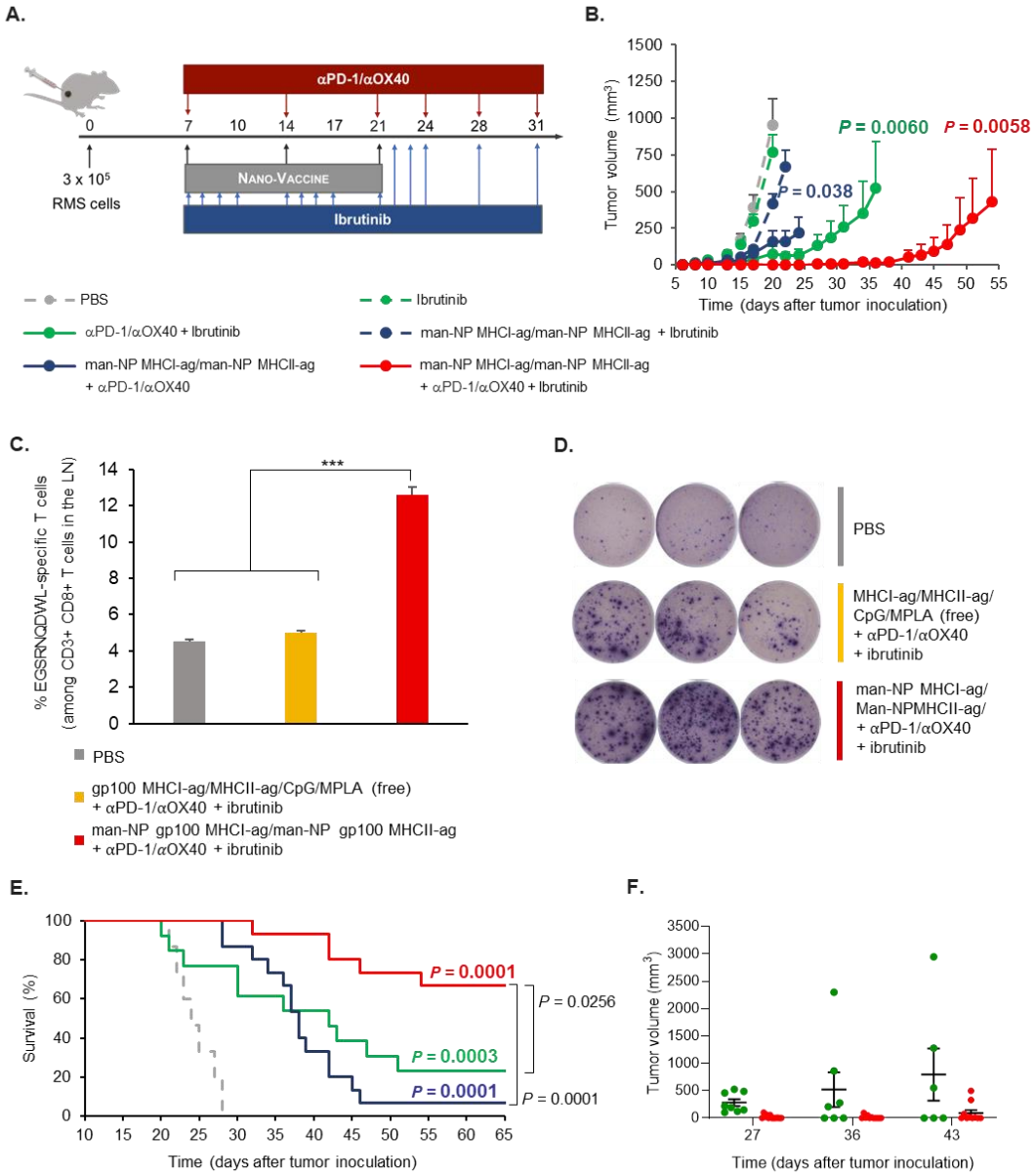

Fig. 5. Trivalent combination of mannosylated nano-vaccines with ibrutinib and αPD-1/αOX40 strongly restricts melanoma growth, leading to long-term survival. A. Timeline of tumour inoculation and treatments. **B.** Tumour growth curve. Data are presented as mean ± SEM (*N* = 7). *P* values correspond to tumour volume at day 20 after tumour inoculation. **C.** Percent of EGSRNQDWL (gp100)-specific $CD8^+$ T cells in the lymph nodes (LN). **D.** ELISpot representative images of IFN-γ spot forming cells among splenocytes after *ex vivo* re-stimulation with melan-A/MART-1 peptides on day 22. **E.** Kaplan-Meier overall survival over time

graph, for mice inoculated with 3 x 10^5 RMS (*N* = 13-15). **F.** Individual tumour volume at days 27, 36 and 43 after tumour inoculation, with mean ± SEM represented (*N*=13-15). All data are presented as mean of 3 independent replicates. * $P < 0.05$; ** $P < 0.01$; *** $P < 0.001$.

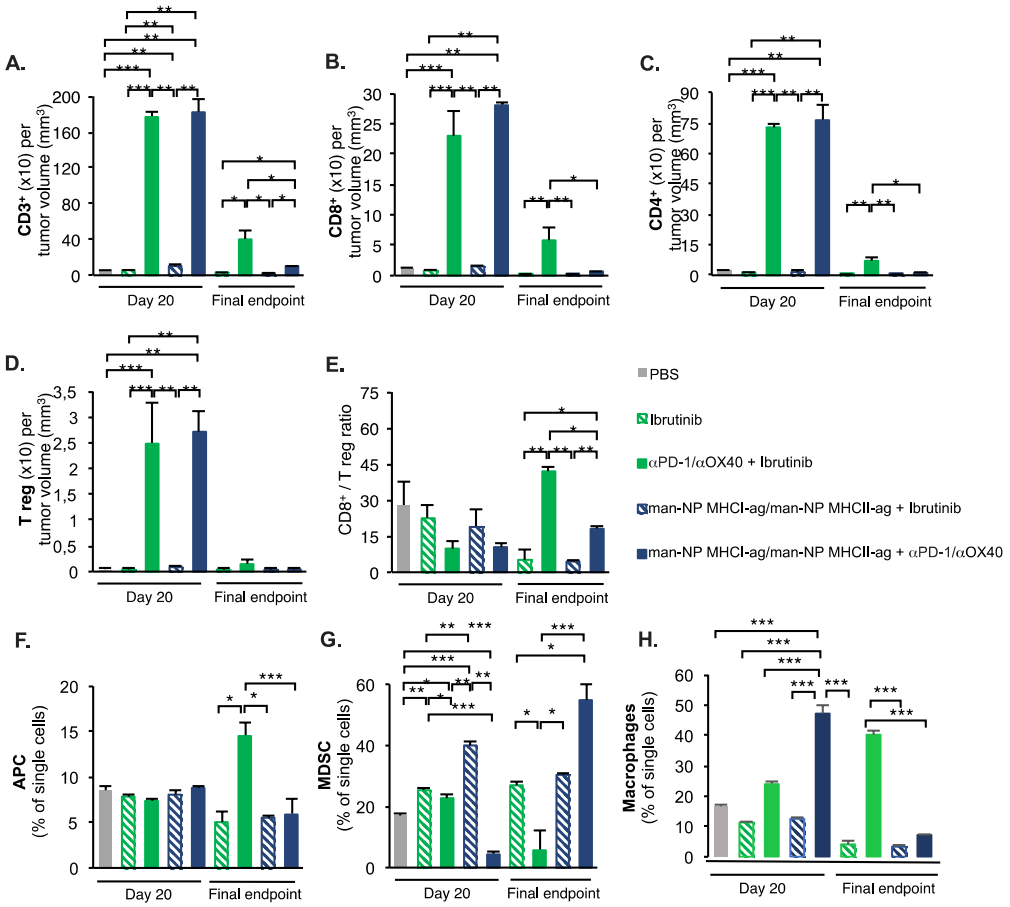

Fig. 6. High CD8⁺/Treg ratio and inhibition of MDSC are associated with improved therapeutic efficacy. A.-H. Tumour-infiltrating immune cell populations. Tumours were isolated on the first endpoint, day 20 after tumour cell inoculation ($N \geq 3$), and at the tumour size-matched second endpoint: day 27 for PBS, ibrutinib only and nano-vaccines + ibrutinib; day 35 for αPD-1/αOX40 + ibrutinib and nano-vaccines + αPD-1/αOX40. Quantification was performed by flow cytometry. Data are presented as mean ± SD of 3 independent replicates. * $P < 0.05$; ** $P < 0.01$; *** $P < 0.001$.

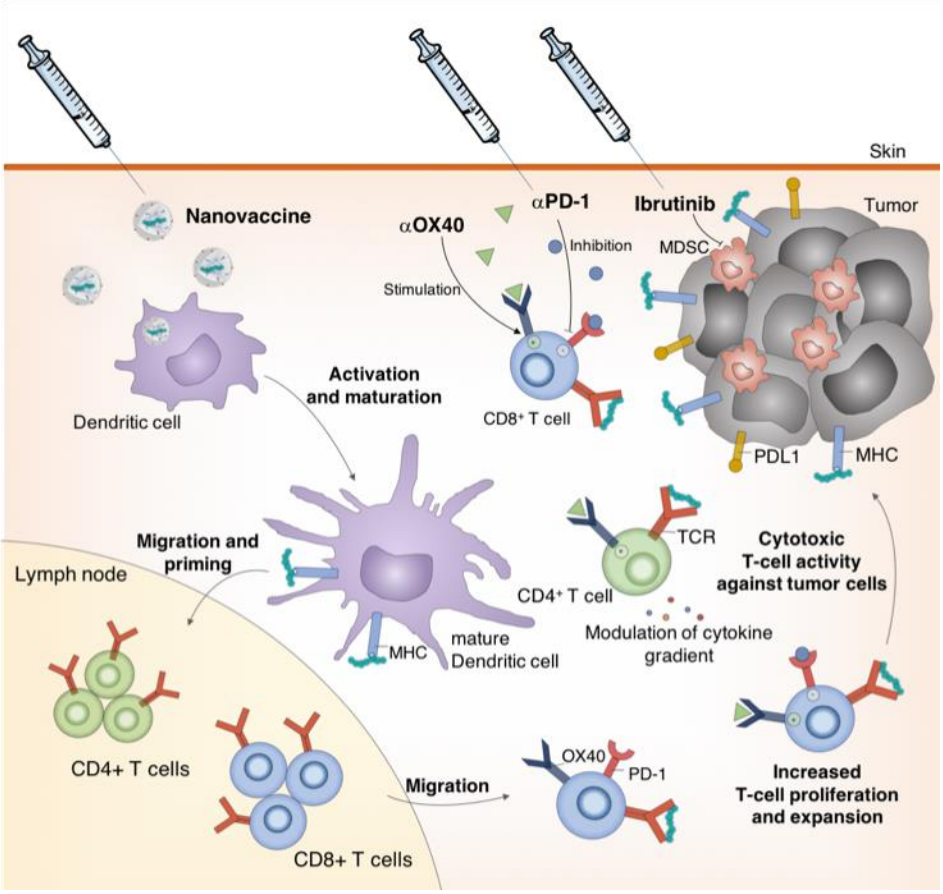

Fig. 7. Proposed model for the trivalent therapeutic strategy combining mannosylated nano-vaccines with ibrutinib and αPD-1/αOX40.